Journal of Advances in Modeling Earth Systems

RESEARCH ARTICLE
10.1029/2018MS001280

A Linear Response Framework for Radiative-Convective Instability

Tom Beucler[1], **Timothy Cronin**[1], **and Kerry Emanuel**[1]

[1]Lorenz Center, Department of Earth Atmospheric and Planetary Sciences, Massachusetts Institute of Technology, Cambridge, MA, USA

Key Points:
- We combine linear responses of diabatic heating with the weak temperature gradient approximation to analyze radiative-convective instability
- The stability of radiative-convective equilibrium to moisture perturbations depends on how heating is converted into vertical moisture advection
- Although clear-sky radiative heating is potentially destabilizing, the convective response to moisture dominates the linear stability problem

Correspondence to:
T. Beucler,
tom.beucler@gmail.com

Citation:
Beucler, T., Cronin, T., & Emanuel, K. (2018). A linear response framework for radiative-convective instability. *Journal of Advances in Modeling Earth Systems*, *10*, 1924–1951. https://doi.org/10.1029/2018MS001280

Received 14 JAN 2018
Accepted 30 MAY 2018
Accepted article online 26 JUN 2018
Published online 13 AUG 2018

Abstract Radiative-convective equilibrium is a simple paradigm for the tropical climate, in which radiative cooling balances convective heating in the absence of lateral energy transport. Recent studies have shown that a large-scale circulation may spontaneously develop from radiative-convective equilibrium through the interactions among water vapor, radiation, and convection. This potential instability, referred to as radiative-convective instability, may be posed as a linear stability problem for the water vapor profile by combining a linear response framework with the weak temperature gradient approximation. We design two analytic models of convective linear response to moisture perturbations, which are similar to Betts-Miller and bulk-plume convection schemes. We combine these convective responses with either clear-sky gray or real-gas radiative responses. In all cases, despite consistent radiative feedbacks, the characteristics of convection dominate the vertical structure of the most unstable linear mode of water vapor perturbations. For Betts-Miller convection, the stability critically depend on a key parameter: the heating to advection of moisture conversion rate (HAM); warmer atmospheres with higher HAM exhibit more linear instability. In contrast, bulk-plume convection is stable across temperatures but becomes linearly unstable with a moisture mode peaking in the midtroposphere once combined to radiation, with approximate growth rates of 10 days.

1. Introduction

Radiative-convective equilibrium (RCE) is the state of the atmosphere in which convective heating balances radiative cooling without lateral transport of moisture or energy (e.g., review by Ramanathan & Coakley, 1978). Although RCE is a natural basic state for the tropical atmosphere, its stability to small water vapor perturbations remains poorly understood, because of the complexity of the interaction among atmospheric water vapor, clouds, radiation, and convection. Water vapor directly interacts with radiation by changing the local emissivity of the atmosphere and the vertical structure of atmospheric radiative cooling. Furthermore, water vapor indirectly interacts with radiation by influencing the formation of clouds. Both of these interactions have the potential to amplify water vapor perturbations: they have been found to be important for spontaneous cyclogenesis (e.g., Wing et al., 2016), and the self-aggregation of convection, through mechanism denial experiments (e.g., Bretherton et al., 2005; Holloway & Woolnough, 2016; Muller & Held, 2012) and energy budgets (e.g., Wing & Emanuel, 2014; Wing & Cronin, 2016). These interactions depend on temperature (e.g., Beucler & Cronin, 2016; Emanuel et al., 2014), clouds, and the structure of the moisture perturbation (e.g., Beucler & Cronin, 2016), making them inseparable from atmospheric convection. The interaction between water vapor and convection has been studied in the contexts of the Madden-Julian oscillation (e.g., Grabowski & Moncrieff, 2004; Hannah & Maloney, 2011) and the self-aggregation of convection in convection-permitting models (e.g., Muller & Bony, 2015; Tompkins, 2001). The unstable nature of this interaction has been referred to as the moisture-convection feedback, and its physics remain unclear. This feedback could rely on updrafts being less cooled by entrainment in a moist environment (e.g., Holloway & Neelin, 2009; Mapes & Neale, 2011; Tompkins, 2001), or on an anomalously moist boundary layer favoring convection by increasing local buoyancy (e.g., Wing et al., 2017). Because these interactions have been diagnosed from nonlinear numerical models, their physical mechanisms are intertwined and hard to interpret, motivating the following question:

What physical mechanisms govern the interactions between water vapor and convection, and between water vapor and radiation, and how do these interactions affect the evolution of a water vapor perturbation?

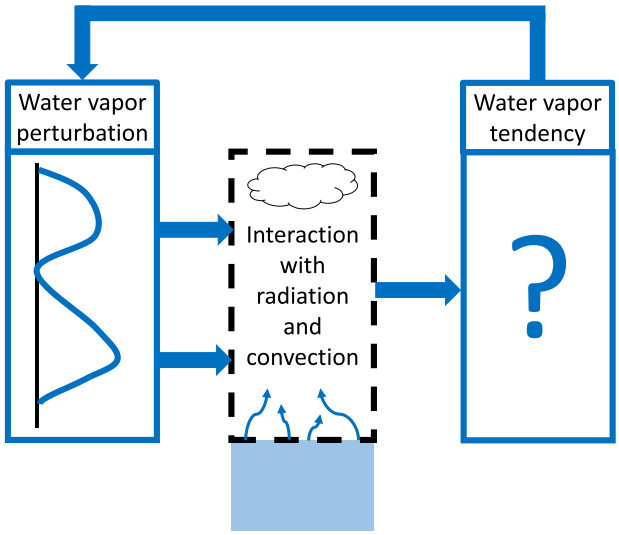

Figure 1. The interaction of a water vapor perturbation with atmospheric radiation and convection leads to a water vapor tendency that can amplify, damp, or move the perturbation.

In this paper, we use a bottom-up approach to diagnose the physics of the interactions among water vapor, radiation, and convection, near a basic state of RCE. To keep the problem tractable, we neglect cloud-radiation interactions and focus on clear-sky radiation. By examining the effect of a water vapor perturbation on both atmospheric convection and radiation, we predict how a water vapor perturbation would evolve over a time scale of ∼10 days (Figure 1). We adopt a linear response approach to quantitatively evaluate the separate contributions from convective heating and moistening, as well as from longwave and shortwave radiative heating. We parametrize large-scale dynamics by using the weak temperature gradient (WTG) framework (e.g., Sobel et al., 2001), where temperatures are fixed and the net residual heating from convection and radiation drives large-scale vertical motions. Each section of this paper addresses a separate question: (Section 2) How can the water vapor tendency profile be computed from the water vapor perturbation profile in the weak temperature gradient framework? (Section 3) How does atmospheric convection linearly respond to water vapor perturbations? (Section 4) How does atmospheric radiation linearly respond to water vapor perturbations? (Section 5) How do small water vapor perturbations evolve as a consequence of their influences on atmospheric radiation and convection?

Sections 3 to 5 can be read independently, and cross-references are included when necessary.

2. Linear Response Framework

2.1. Linear Response Function

This section aims to relate the evolution of a small water vapor perturbation to its effects on radiative and convective diabatic tendencies. For that purpose, we consider a nonrotating atmospheric domain that is large enough (e.g., 100 km in the Tropics) to include both a small cloudy area with deep convective ascent (typically a few percent of the total domain, e.g., Bjerknes, 1938; Malkus et al., 1961), and a large clear area with slow subsidence.

Following Arakawa and Schubert (1974) and Yanai et al. (1973), we assume that the domain's dry static energy s (defined as the sum of the sensible heat and the potential energy, e.g., Yanai et al., 1973) and specific humidity q can both be approximated by their clear-sky values. Furthermore, the domain is assumed to be much smaller than the Rossby radius of deformation and the timescale much longer (e.g., 1 day) than the gravity wave adjustment timescale, so that the WTG approximation holds in the free troposphere. Examples of strict WTG in the literature include the neglect of the free-tropospheric temperature tendency in section 4 of Sobel and Bretherton (2000) or below equation 2 of Sobel and Gildor (2003), and the neglect of ΔT except for the radiative perturbation in equation A4d of Adames and Kim (2016). Here the strict version of the WTG approximation allows us to neglect the local tendency of dry static energy ($\partial s/\partial t = 0$, where t represents time).

The domain-averaged free-tropospheric budgets of dry static energy and specific humidity are then given by the following:

$$\begin{aligned} \omega\frac{\partial s}{\partial p} &= g\left(\frac{\partial \mathcal{F}_{\mathrm{DSE}}}{\partial p}+\frac{\partial \mathcal{F}_{\mathrm{LW}}}{\partial p}+\frac{\partial \mathcal{F}_{\mathrm{SW}}}{\partial p}\right), \\ \frac{\partial q}{\partial t}+\vec{u}\cdot\vec{\nabla}q+\omega\frac{\partial q}{\partial p} &= \frac{g}{L_v}\frac{\partial \mathcal{F}_{\mathrm{LH}}}{\partial p}, \end{aligned} \tag{1}$$

where $\vec{u}$ is the large-scale horizontal velocity, $\vec{\nabla}$ the horizontal gradient operator, ω the large-scale vertical velocity (in units of Pa/s), defined as the area-weighted average of the ascending motion in the cloudy zone and the subsidence motion in the clear-sky zone, p the atmospheric pressure and g is the gravitational acceleration. $\mathcal{F}_{\mathrm{DSE}}$ is the convective dry static energy flux, $\mathcal{F}_{\mathrm{LW}}$ the net longwave flux, $\mathcal{F}_{\mathrm{SW}}$ the net shortwave flux, and $\mathcal{F}_{\mathrm{LH}}$ the convective latent heat flux, all defined in units of W/m^2. The evaporation and condensation rates of hydrometeors are included in the convective heating and moistening tendencies. L_v is the latent heat of vaporization of water vapor, and we neglect the latent heat of fusion. RCE is defined as the the statistically steady state of the previous equations ($\partial/\partial t = 0$), with no large vertical velocity $\left(\vec{\nabla},\omega\right) = \left(\vec{0},0\right)$. From now on, we denote deviations from RCE with primes (X'), while unprimed variables (X) denote RCE. We linearize the previous equation about the basic state, RCE, by assuming that the deviations X' are small compared to the basic-state statistical mean $\overline{X}$. Assuming that the WTG approximation strictly holds for deviations from RCE, the linearized version of equation (1) is

$$\begin{aligned} \omega'\frac{\partial s}{\partial p} &= g\left(\frac{\partial \mathcal{F}'_{\mathrm{DSE}}}{\partial p}+\frac{\partial \mathcal{F}'_{\mathrm{LW}}}{\partial p}+\frac{\partial \mathcal{F}'_{\mathrm{SW}}}{\partial p}\right), \\ \frac{\partial q'}{\partial t}+\omega'\frac{\partial q}{\partial p} &= \frac{g}{L_v}\frac{\partial \mathcal{F}'_{\mathrm{LH}}}{\partial p}. \end{aligned} \tag{2}$$

Combining the two previous equations in order to eliminate ω' relates the evolution of the perturbation specific humidity to the perturbation fluxes:

$$\underbrace{\frac{\partial q'}{\partial t}}_{\text{Moisture tendency}} = \frac{g}{L_v}\left[\underbrace{\frac{\partial \mathcal{F}'_{\mathrm{LH}}}{\partial p}}_{\text{Convective moistening}} + \alpha\left(\underbrace{\frac{\partial \mathcal{F}'_{\mathrm{DSE}}}{\partial p}}_{\text{Convective heating}} + \underbrace{\frac{\partial \mathcal{F}'_{\mathrm{LW}}}{\partial p}}_{\text{Longwave heating}} + \underbrace{\frac{\partial \mathcal{F}'_{\mathrm{SW}}}{\partial p}}_{\text{Shortwave heating}}\right)\right], \tag{3}$$

where we have introduced the nondimensional parameter α that relates heating sources to vertical advection of water vapor:

$$\alpha \overset{\text{def}}{=} -\frac{L_v\partial q/\partial p}{\partial s/\partial p} > 0. \tag{4}$$

This parameter has been previously introduced by Chikira (2014), studied in the context of the Madden-Julien oscillation moisture-convective feedback in Wolding et al. (2016), and corresponds to the ratio $-M_q/M_s$ in equations 1 and 2 of Sobel and Gildor (2003). From now on, we refer to α as the heating-to-advection-of-moisture (HAM) conversion factor (it is positive definite so long as dry static energy increases with height and specific humidity decreases with height). HAM is essentially an exchange rate between the heating rate and the latent heat tendency in WTG; a value greater than 1 indicates that 1 W/kg of heating will translate into more than 1 W/kg of latent heat tendency due to vertical advection by WTG-derived vertical motion. Since $\alpha \overset{\text{def}}{=} 1-(\partial \mathrm{MSE}/\partial p)\,(\partial s/\partial p)^{-1}$, where $\mathrm{MSE} \overset{\text{def}}{=} s + L_v q$ is the moist static energy, a decrease of moist static energy with height implies $\alpha > 1$, whereas an increase of moist static energy with height implies $\alpha < 1$. Tropical profiles of moist static energy generally have a "C" shape of moist static energy with a midtropospheric minimum; $\alpha > 1$ below this minimum and $\alpha < 1$ above it. $1-\alpha$ is closely related to the local definition of normalized gross moist stability (see equation 2 of Kuang, 2012), which usually corresponds to convective amplification when negative through the net import of moisture in the lower

troposphere. Finally, although we will assume a base RCE state for the rest of this study, this framework could be generalized to a base state with mean velocity $\left(\overrightarrow{\overline{u}}, \overline{\omega}\right)$ by adding $\overrightarrow{\overline{u}} \cdot \overrightarrow{\nabla q} + \overline{\omega}\partial q/\partial p$ on the left-hand side of the moisture equation (1), $\overrightarrow{\overline{u}} \cdot \overrightarrow{\nabla q'} + \overline{\omega}\partial q'/\partial p$ on the left-hand side of the moisture equation (2), and $-\overrightarrow{\overline{u}} \cdot \overrightarrow{\nabla q'} - \overline{\omega}\partial q'/\partial p$ on the right-hand side of equation (3).

In summary, equation (3) states that under the WTG approximation, specific humidity is changed directly by the local perturbation convective moistening, and also by the local perturbation convective, longwave and shortwave heating rates through the effect they have on the large-scale vertical velocity. Furthermore, equation (3) gives a framework to study the linear instability of water vapor perturbations. RCE is an equilibrium state, meaning that the right-hand side of equation (3) is zero in RCE. Therefore, the behavior of small water vapor perturbations is determined by the value of the Jacobian in RCE (as long as it does not have eigenvalues with zero real parts, e.g., Hartman, 1960):

$$\frac{\partial}{\partial q'}\left[\frac{\partial q'}{\partial t}\right]_{\mathrm{RCE}} = \frac{g}{L_v}\left[\frac{\partial^2 \mathcal{F}_{\mathrm{LH}}}{\partial p \partial q'} + \alpha\left(\frac{\partial^2 \mathcal{F}_{\mathrm{DSE}}}{\partial p \partial q'} + \frac{\partial^2 \mathcal{F}_{\mathrm{LW}}}{\partial p \partial q'} + \frac{\partial^2 \mathcal{F}_{\mathrm{SW}}}{\partial p \partial q'}\right)\right]_{\mathrm{RCE}}, \tag{5}$$

where the subscript RCE means that the bracketed quantities are evaluated in RCE, in which $q' = 0$ by definition. Equation (5) is the WTG continuous version of equations 7 and 25 of Emanuel et al. (2014), respectively valid for a finite number of layers and two layers. If the Jacobian has at least one eigenvalue with positive real part, RCE may be unstable to small water vapor perturbations. In models and observations, we work on discrete pressure levels, motivating the introduction of the discrete counterpart to the Jacobian: the linear response matrix.

2.2. Linear Response Matrix

We start by defining discrete levels of the atmosphere: $i = 1, 2, \ldots, N$. For short time periods following a small water vapor perturbation, we expect the atmosphere to respond linearly, and the discrete version of equation (5) is

$$\frac{dq'_i}{dt} = \sum_{j=1}^{N} M_{ij} \cdot q'_j, \tag{6}$$

where q'_j is the specific humidity perturbation at a level j, dq'_i/dt the specific humidity tendency in response to that perturbation at a level i, and M the linear response matrix in units s^{-1}, defined as the discrete counterpart of the continuous Jacobian. The linear response function approach has been used by Kuang (2010) to study convectively coupled waves and also by Herman and Kuang (2013) to study the moistening and heating responses of several convective parameterizations. Here the atmospheric temperature profile is fixed, making the linear response function a single two-dimensional matrix rather than a set of four matrices as in the work by Kuang (2010, 2012). The interpretation of our single linear response matrix is described in Figure 2. In a model with equally spaced pressure levels, the column-integrated growth rate of a localized perturbation at level p_j, $\widehat{M}_j$ (in s^{-1}) may be directly computed from the linear response matrix:

$$\widehat{M}_j = \sum_{i=1}^{N} M_{ij}. \tag{7}$$

Using this matrix, we can predict the evolution of the structure and magnitude of a small water vapor perturbation $q'_i(t)$ as

$$q'_i(t) = (\exp Mt)_{ij} \cdot q'_j(t = 0) \tag{8}$$

for small times, where we have exponentiated the linear response matrix:

$$\exp Mt \overset{\mathrm{def}}{=} \sum_{n=0}^{\infty} \frac{(Mt)^n}{n!}.$$

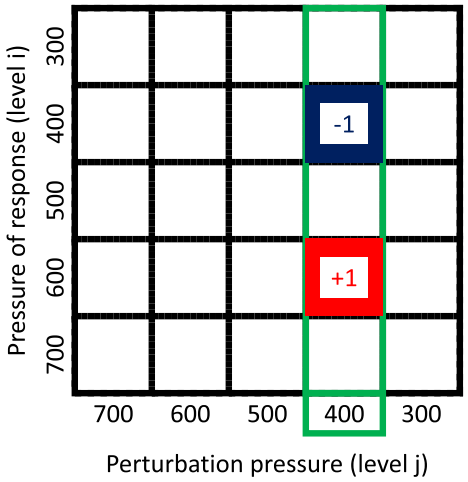

Figure 2. Guide to reading the linear response matrix M: The horizontal axis is the pressure at which water vapor is perturbed (p_j, in hPa), while the vertical axis is the pressure of the water vapor response (p_i, in hPa). In the example depicted above, water vapor is perturbed at $p_j = 400$ hPa, and the water vapor tendency response can be read in the green column. At the local perturbation level $p_i = 400$ hPa, a negative matrix element indicates that a perturbation would decay in time; below the perturbation level at $p_i = 600$ hPa, a positive matrix element indicates that a perturbation would amplify in time. In this simple case, a water vapor perturbation at 400 hPa would be moved to 600 hPa at a unit rate.

If M has at least one eigenvalue with positive real part, RCE may be unstable to a small initial perturbation $q_j'(t=0)$. From equation (6), we see that equal moist and dry perturbations yield opposite responses, which is a consequence of using a linear framework. Therefore, an atmospheric model should produce symmetric responses to opposite-signed perturbations if it is working in its linear range, which allows testing of the linear assumption (e.g., appendix B1 of Herman & Kuang, 2013). In order to gain more insight into the interactions among water vapor, radiation, and convection, we decompose M into four components by writing the discrete counterpart of equation (5):

$$\underbrace{M}_{\text{Linear response}} = \underbrace{M_{\text{LH}} + M_{\text{DSE}}}_{\text{Convective response}} + \underbrace{M_{\text{LW}} + M_{\text{SW}}}_{\text{Radiative response}}, \tag{9}$$

where M_{LH} is the convective moistening response, M_{DSE} the convective heating response, M_{LW} the longwave heating response, and M_{SW} the shortwave heating response. We have incorporated the evaporation and condensation of hydrometeors in the convective response, which is valid as long as the perturbations are small enough not to saturate the domain at any level. Because the atmosphere is assumed to be close to RCE, there is no advective response on the right-hand side of equation (9). In RCE, gross moist stability (see Inoue & Back, 2015; Yu et al., 1998) is undefined, as there is no horizontal flow ($\vec{u} = 0$). However, once the system is perturbed, gross moist stability is internally determined by the vertical structure of the perturbation. If this internally determined gross moist stability is negative, a column-integrated moist static energy perturbation may grow spontaneously, potentially indicating an unstable moisture-convection feedback. Some such scenarios of unstable moisture-convection feedback would be unphysical, if they occurred from a basic state with zero moist available potential energy. This could happen because of limitations of both the strict WTG approximation and convective parameterizations, neither of which necessarily enforces the physical requirement that circulations develop due to conversion of available potential energy to kinetic energy. The definition of moist available potential energy (e.g., Stansifer et al., 2017) is subtle, however, and further consideration of such possible unphysical moisture-convection instabilities is left as a subject for future work. We will now proceed to compute the linear response matrix in idealized and numerical models of convection and radiation.

3. Linear Response of Convection

The goal of this section is to gain physical insight into the linear convective response, defined as the sum of the convective moistening response M_{LH} and the convective heating response M_{DSE}. For that purpose, we analyze

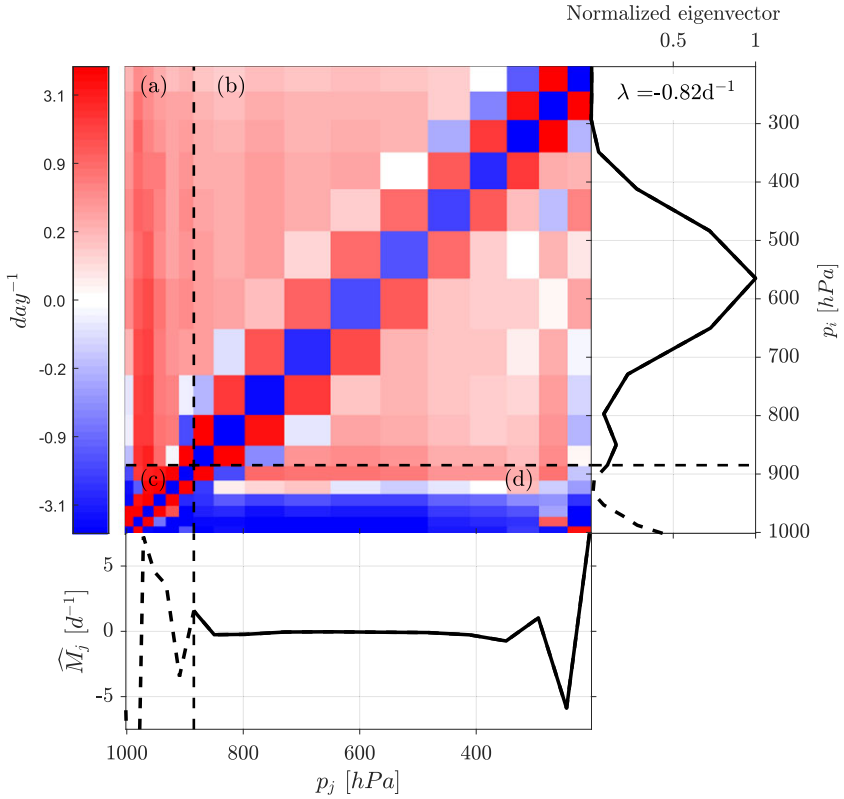

Figure 3. Linear convective matrix from the linear response matrices of Kuang (2012), where the HAM has been evaluated from the mean state of the simulation. The top of the boundary layer, identified as the relative humidity maximum in the lower troposphere, is indicated with dashed black lines. (Bottom panel) Vertically integrated growth rate ($\widehat{M}_j$ in day^{-1}). (Right panel) Eigenvector corresponding to the leading eigenvalue real part λ, normalized to have a maximum of 1.

realistic convective responses from cloud-permitting simulations, before calculating analytic WTG linear convective responses based on toy models of convection similar to two widely used convective schemes.

3.1. Convection in Cloud-Permitting Models

3.1.1. Linear Response Matrix of a Cloud-Permitting Model

We start by analyzing realistic linear response matrices derived from a cloud-permitting model and provided by Zhiming Kuang following the methodology he described in Kuang (2010). The System for Atmospheric Modeling (SAM; Khairoutdinov & Randall, 2003) is run to RCE in a 128 × 128km^2 square domain with 2-km horizontal resolution and 28 vertical levels, as described in section 4 of Kuang (2012). Kuang (2012) ran all simulations using a surface temperature of 301.15K, and integrated the perturbed runs for as long as 10,000 days to minimize the noise level of the linear response matrices. We calculate the WTG convective response matrix by adapting equation 3 to the convective responses of moisture to moisture perturbations $\left(dq/dt \text{ from } q'\right)$ (in s^{-1}) and temperature to moisture perturbations $\left(dT/dt \text{ from } q'\right)$ (in K/s per kg/kg) (respectively Figures 8b and 8c from Kuang, 2012):

$$\underbrace{M_{\mathrm{LH}}}_{\text{Convective moistening}} = \left(\frac{dq}{dt} \text{ from } q'\right) \quad | \quad \underbrace{M_{\mathrm{DSE}}}_{\text{Convective heating}} = \alpha \frac{c_p}{L_v}\left(\frac{dT}{dt} \text{ from } q'\right), \tag{10}$$

where c_p is the specific heat capacity of dry air at constant pressure and the HAM α is calculated from the mean thermodynamic profiles of the SAM RCE simulation of Kuang (2012). The linear convective response, sum of the convective moistening and heating responses, is depicted in Figure 3. We subdivide the convective linear response into four regions:

(a) The strong free-tropospheric convecting heating resulting from boundary-layer moisture perturbations,
(b) The free-tropospheric convective heating and moistening responses to free-tropospheric moisture perturbations,

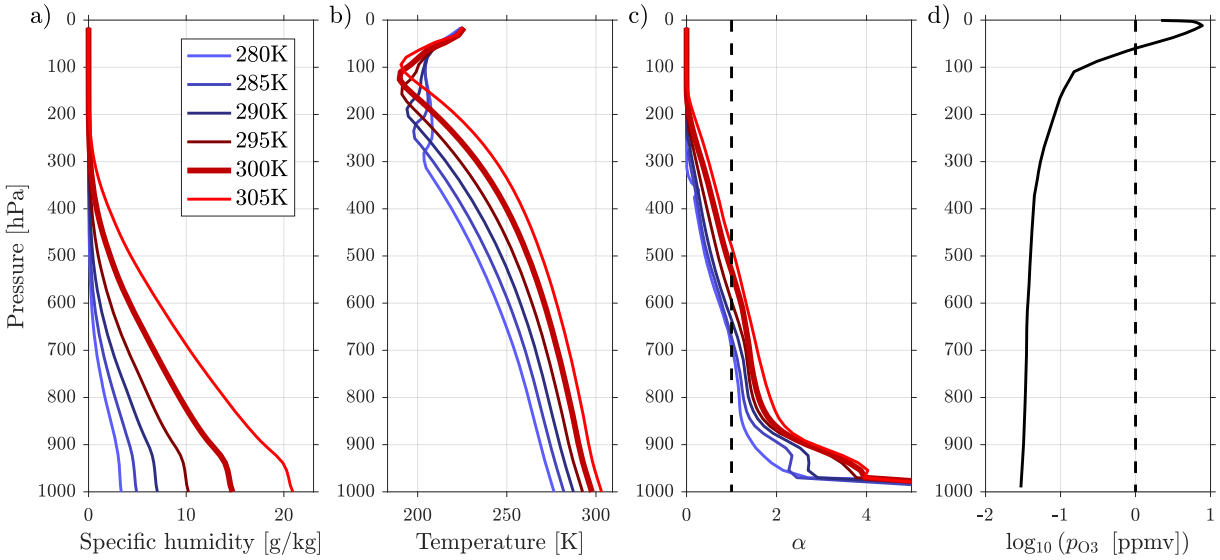

Figure 4. Vertical profiles of (a) specific humidity (in g/kg), (b) temperature (in K), (c) HAM, and (d) log 10 of the ozone volume concentration (in ppmv) in the SAM simulations ran by Tristan Abbott.

(c) The local response to boundary-layer moisture perturbations (dominated by water vapor mixing), and
(d) The cooling and drying of the boundary layer resulting from free-tropospheric moisture perturbations.

Although combining convective heating and moistening responses into a single WTG response is always mathematically possible, it does not directly inform us on the evolution of water vapor perturbations in the boundary layer where WTG breaks down because of horizontal buoyancy gradients (regions a, c, and d). In this study, we focus on explaining the free-tropospheric response to free-tropospheric perturbations (region b) and its consequences for the linear stability of water vapor perturbations. It is possible to separate the convective response into three separate components:

1. A local drying of moisture perturbations (blue diagonal), with strong local mixing of water vapor (red squares right above and right below the blue diagonal),
2. A tropospherically uniform convective heating, which decreases with height due to the modulation by the HAM profile (red lower-right triangle and small part of the red upper-left triangle), and
3. A combination of convective heating and moistening above the diagonal (most of the red upper-left triangle).

The combination of these three components leads to a stable convective response in RCE (the leading real eigenvalue is $-0.82\,\mathrm{day}^{-1}$), consistent with the stability of RCE in Kuang's cloud-permitting simulations. Constructing convective responses and combining them with radiative responses for a variety of basic states is computationally expensive and difficult to interpret in cloud-permitting simulations. Therefore, we proceed to the construction of simple convective responses that mimic the two components of more realistic responses. Before doing so, we calculate different basic RCE states for our simple convective models from cloud-permitting simulations.

3.1.2. RCEs From Cloud-Permitting Simulations

To provide basic states of temperature and specific humidity, we use simulations of RCE conducted by Tristan Abbott on the Engaging computational cluster at MIT, using version 6.10.6 of the SAM cloud-permitting model. The surface temperature varies from 280 to 305 K in increments of 5 K between simulations. The horizontal domain is 96×96 grid cells with 1-km horizontal resolution, while the stretched vertical grid has 64 levels, with eight levels below 1 km and 500 m vertical resolution above 3 km. The upper boundary is a rigid lid at 28 km height, and a sponge layer from 19 to 28 km prevents excessive gravity wave reflection off of the top of the model domain. Insolation is set to an equinoctial diurnal cycle at 19.45° north, producing a time-mean insolation of $413.6\,\mathrm{W/m^2}$. We use the radiation code from the National Center for Atmospheric Research Community Atmosphere Model version 3 Collins et al. (2006) and set the carbon dioxide mixing ratio to 355 ppmv, and the ozone mixing ratio to the standard tropical profile in SAM in all simulations. Microphysics are parameterized with the SAM single-moment microphysics scheme, documented in

Khairoutdinov and Randall (2003). No large-scale forcing of winds, temperature, or moisture is imposed in any simulations. In these simulations, convection remains disaggregated (referred to as "pop-corn" convection), and the thermodynamic profiles (shown in Figure 4) are averaged in space and time over 60 days after a 40-day spin-up. The column water vapor varies from 7.9 to 68.7 kg/m^2 from the coldest to warmest surface temperature (Figure 4a). The temperature profile is close to a moist adiabatic profile in the lower troposphere and progressively approaches a dry adiabat near the tropopause (Figure 4b). Finally, the HAM profile is very large in the boundary layer (with values up to 10 near the surface), decreases below 1 in the lower to midtroposphere before asymptoting to 0 near the tropopause (Figure 4c). Only the warmest surface temperature has a free-tropospheric-averaged α larger than 1. The reference simulation for sections 3 and 4 uses a surface temperature of 300 K and is denoted with a thicker line in Figure 4. Its column water vapor is 44.5 kg/m^2, column relative humidity 84%, tropopause pressure 121hPa, tropopause temperature 190 K, and its HAM has a mean free-tropospheric value of 0.91. The standard tropical ozone profile in SAM (Figure 4d) has a column ozone of 5.3 g/m^2; its mixing ratio reaches a minimum of 30 ppbv at the surface and a maximum of 7.8 ppmv in the upper atmosphere.

3.1.3. Toy Models of Convective Response

Starting from the 300K reference simulation, we construct Betts-Miller-like and bulk-plume-like convective linear responses, with our schemes designed so that tendencies of water vapor and temperature are zero in the reference state. The two toy models provide meaningful linear responses about the same basic state under the WTG approximation, responses we can then directly compare. For brevity, we refer to the 2 toy models as simply "Betts-Miller" and "bulk-plume" schemes, keeping in mind that we have chosen toy models over their more realistic counterparts and traded realism for analytical tractability. Since the eigenvalues of radiative-convective instability are very sensitive to the convective response, this choice is a first step that provides novel physical insight.

3.2. Betts-Miller Scheme

3.2.1. Description

The Betts-Miller (1986, 1993) convective scheme, commonly used as a minimal model of moist convection (e.g., Frierson, 2007), computes precipitation and convective tendencies based on the deviation of the temperature and water vapor profiles from reference values in a convectively unstable atmosphere. In the free troposphere, the scheme relaxes moisture and temperature perturbations to zero in time τ_{BM}, where τ_{BM} is a parameter of the scheme (typically a few hours). In order to conserve the moist static energy of the convecting layer, the scheme shifts the temperature profile in time τ_{BM}, by a uniform amount $(\Delta T)_{\mathrm{BM}}$ given by

$$(\Delta T)_{\mathrm{BM}} = \frac{1}{c_p\left(p_b - p_t\right)} \int_{p_t}^{p_b} \left(c_p T_{\mathrm{BM}} + L_v q_{\mathrm{BM}}\right), \tag{11}$$

where c_p is the specific heat constant of dry air at constant pressure, L_v the latent heat of vaporization of water vapor, p_b the pressure at the top of the planetary boundary layer, p_t the tropopause pressure, T_{BM} the temperature perturbation from the Betts-Miller reference profile, and q_{BM} the specific humidity perturbation from the Betts-Miller reference profile.

3.2.2. Linear Response

The theoretical framework of section 2 provides two simplifying constraints. First, we can linearize equation (11) about RCE and note that $\left(T'_{\mathrm{BM}}, q'_{\mathrm{BM}}\right) = (T', q')$. Second, under the WTG approximation, the temperature perturbation T' is zero. Since the convective heating is given by the tendency of $(\Delta T)_{\mathrm{BM}}$, its perturbation solely depends on the moisture perturbation q' .

In order to evaluate the linear response of the Betts-Miller scheme, we introduce a water vapor perturbation q'_j in a thin pressure layer $[p_j - \Delta p/2\,,\ p_j + \Delta p/2]$, for which the pressure thickness Δp is much smaller than the pressure level p_j. The pressure level p_j is above the top of the boundary layer, defined as the level of maximal relative humidity (928hPa for the reference profile), and below the tropopause, defined as the level of minimal temperature (188hPa for the reference profile). We assume that the whole atmosphere between these two levels is convecting. In response to the water vapor perturbation q'_j, the scheme relaxes q'_j to zero in time

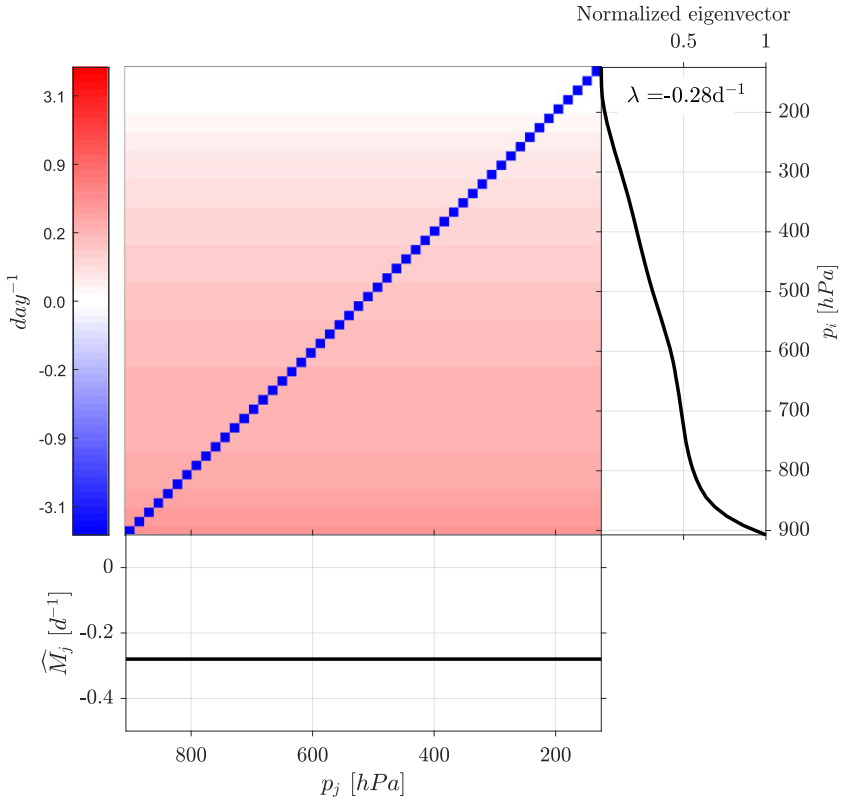

Figure 5. Betts-Miller linear convective matrix for τ_{BM} = 3hr, where the HAM has been evaluated from the reference SAM RCE profile. (Bottom panel) Vertically integrated growth rate ($\widehat{M}_j$ in day^{-1}). (Right panel) Eigenvector corresponding to the leading eigenvalue real part λ, normalized to have a maximum of 1.

τ_{BM}, corresponding to a local damping of the water vapor perturbation. Therefore, the convective moistening response matrix (in units s^{-1}) is given by

$$\left(M_{LH}\right)_{ij} \overset{\text{def}}{=} \frac{1}{q_j'}\left(\frac{dq_i'}{dt}\right)_{BM} = \underbrace{-\frac{\delta_{ij}}{\tau_{BM}}}_{\text{Local drying}}, \tag{12}$$

where i is the response level, j the perturbation level, BM a subscript denoting the action of the Betts-Miller scheme, and δ_{ij} the Kronecker symbol, defined as 1 if $i = j$ and 0 otherwise. In contrast, the convective heating in response to the perturbation moistening is equally distributed over all layers of the atmospheric column, corresponding to the following convective heating response:

$$\left(M_{DSE}\right)_{ij} \overset{\text{def}}{=} \frac{\alpha_i}{L_v q_j'}\frac{c_p\left(\Delta T\right)_{BM}'}{\tau_{BM}} = \underbrace{\frac{\alpha_i}{\tau_{BM}}\frac{\Delta p}{p_b - p_t}}_{\text{Heating everywhere}}, \tag{13}$$

where M_{DSE} is the convective heating response matrix (in units s^{-1}), α_i the HAM (equation (4)) evaluated at the response level p_i, and $\left(p_b - p_t\right)$ the thickness of the free troposphere. Figure 5 represents the convective linear response of the Betts-Miller scheme with SAM RCE profiles as our basic state. Thus, the response of the Betts-Miller scheme to moist perturbations can be separated in two parts:

1. A local convective drying along the diagonal, where perturbations are removed in time τ_{BM}.
2. A tropospherically uniform convective heating which has a growth rate that decreases with height due to modulation by the HAM profile (equation (13)).

3.3. Bulk Plume Equations

3.3.1. Description

Most of the parameterizations that represent precipitating convection use bulk schemes, which model an ensemble of different cumulus elements as a small number of entraining-detraining plumes. Plant (2009) reviews the theoretical basis for different bulk parameterizations and spectral parameterizations (e.g., Arakawa & Schubert, 1974). Here we start with a simplified form of the bulk-plume equations for a single updraft plume developed by Yanai et al. (1973), which has been used by Romps (2014) in order to estimate the moisture profile from specified entrainment, detrainment, and mass flux profiles:

$$-g\frac{\partial m}{\partial p}=e-d, \tag{14}$$

$$-g\frac{\partial\left(mq^{*}\right)}{\partial p}=eq-dq^{*}-c, \tag{15}$$

$$-g\frac{\partial\left(mq\right)}{\partial p}=eq-dq^{*}, \tag{16}$$

$$-g\frac{\partial\left[m\left(s+L_{v}q^{*}\right)\right]}{\partial p}=e\left(s+L_{v}q\right)-d\left(s+L_{v}q^{*}\right), \tag{17}$$

where g is the gravitational acceleration; m is the cloud updraft mass flux (in units $\mathrm{kg\cdot m^{-2}\cdot s^{-1}}$); p is the hydrostatic pressure; (e,d,c) are the entrainment, detrainment, and condensation rates (in units $\mathrm{s^{-1}}$); q^{*} is the saturation specific humidity; and q is the environmental specific humidity. To keep the model analytically tractable, we have neglected thermodynamical details of the bulk plume model, including

1. The weight of the condensate on the right-hand side of the mass equation (14), which is reasonable for small values of q^{*}.
2. The evaporation of condensate on the right-hand side of the environmental moisture equation (16), which assumes that any condensate instantly falls to the surface without re-evaporating in the clear-sky environment. This is a poor approximation to reality, as clear-sky re-evaporation balances the difference between convective heating and radiative cooling in RCE.
3. The difference between the dry static energy of the clouds and the environment (neutral buoyancy assumption if virtual effects are ignored, e.g., Singh & O'Gorman, 2013), which affects the right-hand side of the moist static energy equation (17).
4. The mixing between the neutral air of the troposphere and the stably stratified air of the stratosphere, which can occur through convective overshooting and gravity wave breaking.

3.3.2. Basic State

Assuming that the bulk-plume equations apply, we aim at diagnosing the equilibrium updraft mass flux, detrainment, entrainment and condensation rates from RCE moisture and temperature profiles. In Appendix A1 we show that the bulk-plume equations lead to a unique set of solutions for the equilibrium convective profiles:

$$m\left(p\right)=\frac{\widehat{Q}_{\mathrm{BP}}\cdot\mathcal{I}\left(p\right)}{L_{v}q_{\mathrm{def}}}, \tag{18}$$

$$e\left(p\right)=\frac{g\widehat{Q}_{\mathrm{BP}}\cdot\mathcal{I}\left(p\right)}{L_{v}^{2}q_{\mathrm{def}}^{2}}\frac{\partial\left(s+L_{v}q^{*}\right)}{\partial p}, \tag{19}$$

$$d\left(p\right)=\frac{g\widehat{Q}_{\mathrm{BP}}\cdot\mathcal{I}\left(p\right)}{L_{v}q_{\mathrm{def}}^{2}}\frac{\partial q}{\partial p}, \tag{20}$$

$$c\left(p\right)=-\frac{g\widehat{Q}_{\mathrm{BP}}\cdot\mathcal{I}\left(p\right)}{L_{v}^{2}q_{\mathrm{def}}}\frac{\partial s}{\partial p}, \tag{21}$$

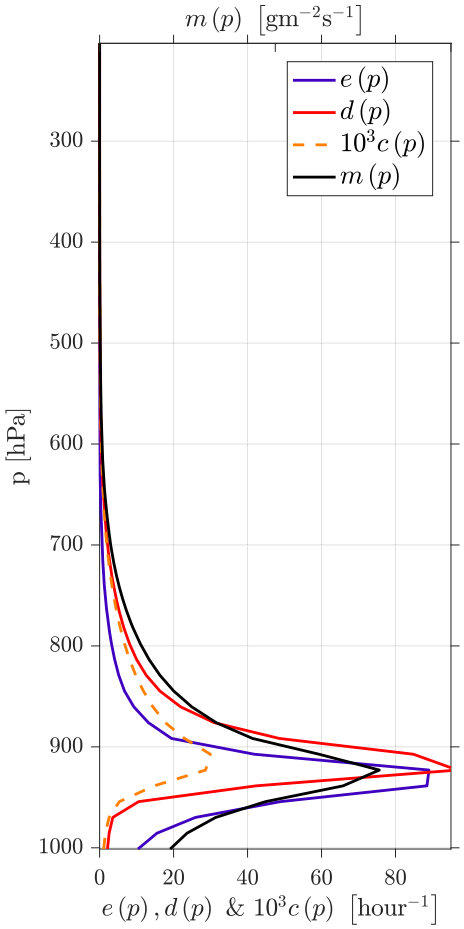

Figure 6. Entrainment and detrainment rate profiles (in hr^{-1}) and condensation rate profile (in month^{-1}) in RCE, as diagnosed from the reference SAM RCE temperature and moisture profiles.

where $\widehat{Q}_{\mathrm{BP}}$ is the total free-tropospheric atmospheric cooling (a free parameter of our simple bulk-plume model), p_b is the pressure at the top of the planetary boundary layer; we have introduced the function $\mathcal{I}$:

$$\mathcal{I}\,(p) \overset{\mathrm{def}}{=} \exp\left[\int_{p_b}^{p} \frac{dp'}{L_v q_{\mathrm{def}}\,(p')} \frac{\partial s\,(p')}{\partial p'}\right],$$

as well as the saturation deficit q_{def}:

$$q_{\mathrm{def}} \overset{\mathrm{def}}{=} (q^* - q)\,. \tag{22}$$

Taking the reference SAM RCE profiles as RCE leads to the convective profiles shown in Figure 6.

Although our simple model model captures the order of magnitude of convective properties overall (e.g., Figures 5 and 6 of Pauluis & Mrowiec, 2013), the entrainment rates can artificially take negative values in the upper troposphere and at the top of the boundary layer, where the saturated moist static energy decreases with height. This limitation of the entrainment diagnostics remains if ice precipitation is taken into account (e.g., equation 22 of Pauluis & Mrowiec, 2013) or if we take into account the weight of condensate and/or the re-evaporation of condensates in the clear-sky environment (not shown). Taking into account troposphere-stratosphere mixing, the preferential detrainment of plumes with low saturated moist static energy, or cloud-top mixing would (at least partly) correct this issue, but these details are beyond the scope of our simple bulk-plume model.

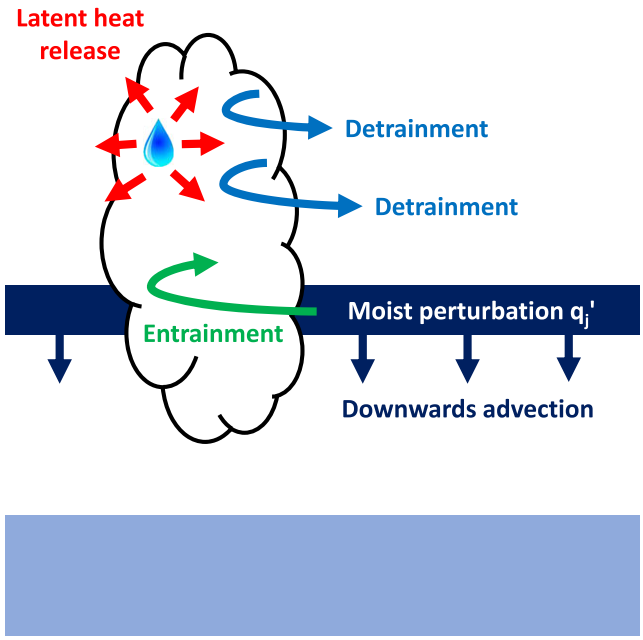

Figure 7. The moist perturbation at level p_j is entrained in the cloudy updraft, where it detrains and releases latent heat through condensation at level $p_{i>j}$ above the perturbed level. The moist perturbation is also advected downwards to level p_{j-1} by the subsidence mass flux.

3.3.3. Linear Response

The steady equations (14)–(17) do not constrain the (time dependent) linear response of our simple bulk-plume model. For simplicity, analytic tractability, and since the moisture perturbations are small and free tropospheric, we assume that the additional water vapor behaves as a passive tracer to evaluate the response of our bulk-plume toy model. Note that this approximation would not be valid in the boundary layer, as shown in panel (a) of Figure 3, nor for large free-tropospheric perturbations that would inhibit or enhance deep convection. This approximation ignores perturbations in the convective ensemble properties (m, e, d, c), which remain at their RCE values computed in section 3.3.2 during the linear response. In a more realistic bulk-plume model, the transient evolution of the system would depend on other equations, such as the mass-flux closure equation. We evaluate this passive tracer linear response in four steps, following Figure 7:

1. We introduce a perturbation q_j' in a thin convecting layer $[p_j - \Delta p/2\ ,\ p_j + \Delta p/2]$, with entrainment: $e_j = e\left(p_j\right)$, where e is the RCE entrainment profile given by equation (19).
2. We assume that the perturbation q_j' is entrained into the convective plume at a rate e_j from the perturbation level p_j and this entrained portion of the water vapor perturbation is communicated to all levels above: $p_i < p_j$.
3. At a given level p_i within the plume, the perturbation q_j' condenses at a rate proportional to the local RCE condensation rate at that level: $c_i = c\left(p_i\right)$ and detrains at a rate proportional to the RCE detrainment rate $d_i q_i^* = \left(dq^*\right)\left(p_i\right)$. The proportionality constant is uniform in the convecting layer and related to the entrainment rate at the perturbation level.
4. Finally, the environmental perturbation is also advected downwards by the local subsidence mass flux $-m_i = -m\left(p_i\right)$.

In Appendix A2, we show that the convective moistening response M_{LH} and the convective heating response M_{DSE} are respectively given by

$$\left(M_{\mathrm{LH}}\right)_{ij} = e_j \left[\underbrace{-\delta_{ij}}_{\text{Entrained moisture}} + \underbrace{\frac{d_i q_i^* \delta_{i>j}}{\sum_{i>j}\left(d_i q_i^* + c_i\right)}}_{\text{Detrained moisture above}} \right] + \underbrace{\frac{g m_j \left[\delta_{i(j-1)} - \delta_{ij}\right]}{\Delta p}}_{\text{Downwards advection}}, \tag{23}$$

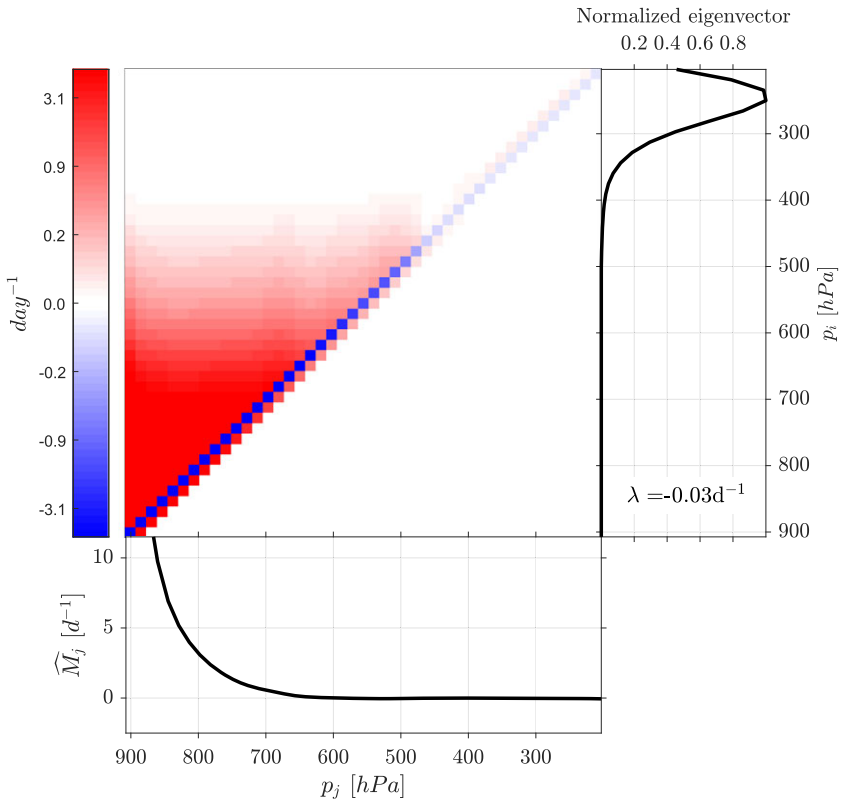

Figure 8. Bulk-plume linear convective matrix ($M_{LH} + M_{DSE}$) for $\widehat{Q}_{BP}$ = 150 W/m^2. (Bottom panel) Vertically integrated growth rate ($\widehat{M}_j$ in day^{-1}). (Right panel) Eigenvector corresponding to the leading eigenvalue real part λ, normalized to have a maximum of 1 (note that the leading eigenvalue here is negative, so it represents the slowest-decaying mode).

$$\left(M_{DSE}\right)_{ij} = \underbrace{\frac{e_j \alpha_i c_i \delta_{i>j}}{\sum_{i>j}\left(d_i q_i^* + c_i\right)}}_{\text{Latent heating above}}, \tag{24}$$

where δ_{ij} is 0 if $i \neq j$ and 1 if $i = j$, $\delta_{i>j}$ is 0 if $i \leq j$ and 1 if $i > j$, and $\delta_{j(i-1)}$ is 0 if $i \neq j-1$ and 1 if $i = (j-1)$.

The linear convective response is depicted in Figure 8, while the separate convective moistening and heating responses are depicted in Figure A1 of Appendix A2. Overall, the response of the bulk-plume scheme to moist perturbations can be separated in three parts:

1. A local drying (blue diagonal) due to the entrainment of water vapor in the plume and its downwards advection by the subsiding mass flux.
2. A growth of the perturbation above the perturbation level (red upper-left part of the matrix) due to the detrainment of the moist plume as well as the latent heating within the plume. This component of the response scales like the detrainment and condensation rate profiles from bottom to top, and like the local entrainment rate profile from left to right.
3. A moistening right below the perturbation level (red below the diagonal) due to the downwards advection of the moist perturbation by the subsidence mass flux.

The Betts-Miller and bulk-plume convective responses both conserve moist static energy: they locally damp the perturbation, and re-distribute it everywhere in the case of the Betts-Miller scheme and upwards in the case of the bulk-plume scheme. Unlike convection, radiation diabatically heats the column, which may enhance moist static energy perturbations even when the HAM profile is uniform (e.g., Beucler & Cronin, 2016).

4. Linear Response of Radiation

In this section, we compute the linear response of longwave radiation M_{LW} and that of shortwave radiation M_{SW} using analytical and real-gas radiative transfer models. We use the same tropical basic state as in section 3.

4.1. Two-Stream Model of Longwave Radiation

The framework introduced here generalizes the analytical framework introduced in Beucler and Cronin (2016) by allowing the water vapor profile to vary freely and writing the differential optical thickness $d\tau$ as a product of a general function f_1 of pressure and a general function f_2 of specific humidity:

$$d\tau = \kappa f_1(p) f_2(q) \frac{dp}{g}, \tag{25}$$

where the gray longwave absorption coefficient κ has the units m^2/kg, and dp is the differential atmospheric pressure. Beucler and Cronin (2016) accounted for pressure broadening of water vapor in a simple fashion by choosing $\kappa = 0.17\ m^2/kg$, $f_1(p) = p/p_s$, $f_2(q) = q$, where p_s is the surface pressure, and we make the same choice in this section. From the two-stream Schwarzschild equation for a one-dimensional plane-parallel atmosphere (equations (10) and (11) of Beucler & Cronin, 2016), we can write the longwave convergence in pressure coordinates $d\mathcal{F}_{LW}/dp$ (in $Wm^{-2}\,hPa^{-1}$) as the product of the longwave convergence in optical thickness coordinates (in W/m^2) with the differential optical thickness (in hPa^{-1}):

$$\frac{d\mathcal{F}_{LW}}{dp} = \frac{d\left(\mathcal{F}_{\uparrow} - \mathcal{F}_{\downarrow}\right)}{dp} = \underbrace{\left(\mathcal{F}_{\uparrow} + \mathcal{F}_{\downarrow} - 2\sigma T^4\right)}_{\text{LW convergence}} \overbrace{\frac{\kappa f_1 f_2}{g}}^{\text{Diff opt thickness}}, \tag{26}$$

where $\mathcal{F}_{\uparrow}$ and $\mathcal{F}_{\downarrow}$ are respectively the upwelling and downwelling radiative fluxes (in W/m^2), σ is the Stefan-Boltzmann constant and T is the atmospheric temperature. In Appendix B, we show that the linear longwave response can be written as the sum of two components:

$$\left(M_{LW}\right)_{ij} = \underbrace{\frac{\kappa \alpha_i}{L_v}\left[f_1\left(\frac{df_2}{dq}\right)_{q=0}\right]_{p_j}}_{\text{Opt thick pert}} \left\{ LW_{\text{local},ij} + \overbrace{\frac{\kappa \Delta p \left(f_1 f_2\right)_{p_i}}{g}}^{\text{Local opt thickness}} LW_{\text{non-local},ij} \right\}. \tag{27}$$

Their general expression and physical interpretation for a moist perturbation $q'_j > 0$ are

1. A local increase in the radiative cooling, due to the increase of the local emissivity:

$$LW_{\text{local},ij} = \left(\mathcal{F}_{\uparrow} + \mathcal{F}_{\downarrow} - 2\sigma T^4\right)_{p_i} \delta_{ij}, \tag{28}$$

2. A nonlocal term that has different signs above and below the perturbation:

$$LW_{\text{non-local},ij} = \underbrace{\exp\left(-\left|\tau_i - \tau_j\right|\right)}_{\text{Transmissivity}} \left[-\left(\mathcal{F}_{\uparrow}\right)_{p_j} \delta_{i>j} - \left(\mathcal{F}_{\downarrow}\right)_{p_j} \delta_{i<j} + \sigma T_j^4 \delta_{i\neq j}\right], \tag{29}$$

where τ_i is the optical thickness of the atmosphere between p_i and space, τ_j is the optical thickness of the atmosphere between p_j and space, and T_j is the atmospheric temperature at the perturbation level. Above the perturbation level ($i > j$), the upwelling flux received from the perturbation $\left(\mathcal{F}_{\uparrow}\right)_{p_j}$ decreases because the moist perturbation absorbs some of the upwelling atmospheric radiation below it. Below the perturbation level ($i < j$), the downwelling flux received from the perturbation $\left(\mathcal{F}_{\downarrow}\right)_{p_j}$ decreases because the moist perturbation absorbs some of the downwelling atmospheric radiation above it. In return, the perturbation

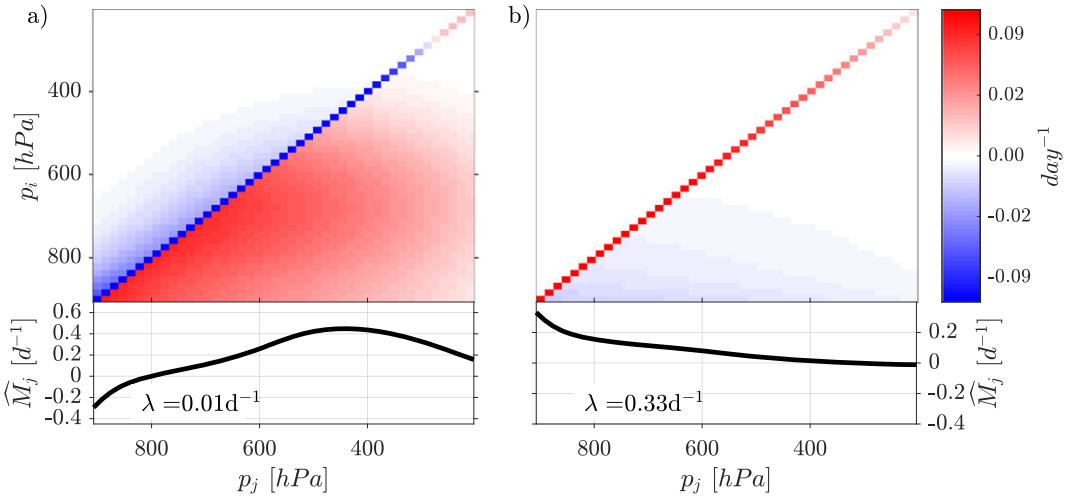

Figure 9. (a) Longwave linear response matrix (in month^{-1}) and vertically integrated longwave growth rate (in day^{-1}) plotted against perturbation level (in hPa). (b) Shortwave linear response and vertically integrated shortwave growth rate. The total optical thickness of the free troposphere is 6 in the longwave and 0.5 in the shortwave. It corresponds to a net free-tropospheric cooling of 215 W/m^2. The analytical matrices, with leading real eigenvalues λ, have both been tested against a numerical version of the two-stream Schwarzschild model.

emits radiative energy up and down at a rate σT_j^4. Because the atmospheric temperature decreases with height, the emission term σT_j^4 exceeds the radiative flux $\left(\mathcal{F}_{\downarrow}\right)_{p_j}$ received from above but is less than the radiative flux $\left(\mathcal{F}_{\uparrow}\right)_{p_j}$ received from below. Therefore, we expect the net longwave convergence to decrease above the perturbation level and to increase below it for a positive moisture perturbation. The amplifying radiative linear response resulting from the nonlocal heating perturbation below a moist perturbation (or cooling perturbation below a dry perturbation) is referred to as the radiative amplification effect.

Figure 9a shows the longwave linear response for a surface optical thickness of 5.4, which matches the net radiative cooling as computed in SAM and is a reasonable tropical value corresponding to column water vapor values of 40 kg/m^2 in the simple model of Beucler and Cronin (2016). The local increase is cooling (LW_{local}) appears as a blue diagonal throughout the troposphere, except near the tropopause where the gray-radiation skin temperature exceeds the atmospheric temperature, leading to local heating and pointing to one limitation of the gray model. The decrease in radiation received from the ground is prevalent in the lower troposphere, and corresponds to the blue area above the bottom left corner of the matrix. The damping linked to the decrease in radiation received from the atmosphere is largest right above and right below the diagonal and explains why the blue zone above the diagonal extends to the midtroposphere. The radiative amplification term is larger than the damping terms and well distributed below the perturbation level. Water vapor molecules below a moist perturbation emit less radiation to space, resulting in a net heating below the perturbation level. For lower-tropospheric perturbations, the three damping terms on the right-hand side of equation (27) are prevalent in the sum, and $\widehat{M}_j < 0$. However, $\widehat{M}_j$ becomes positive in the case of mid to upper-tropospheric perturbations, for which the radiative amplification term is largest. The potential growth of column-integrated perturbations through their unstable interaction with longwave radiation has been extensively studied in Beucler and Cronin (2016), and referred to as moisture-radiative cooling instability. Note that the toy radiative model presented in equation 28 of Emanuel et al. (2014) is a specific case of our gray model in the limit of two optically thin atmospheric layers. This framework provides fundamental understanding for the gray part of the clear-sky real-gas radiative response and gives an idea of the cloud longwave radiative response, for which the gray approximation holds better. The reader interested in the assumptions made in order to compute the optical thickness profile for Figure 9 is referred to Appendix B3.

4.2. One-Stream Model of Shortwave Radiation

Following Beucler and Cronin (2016), we adopt a simple one-stream model of radiation with the generalized optical thickness given by equation (25):

$$\mathcal{F}_{SW} = \mathcal{S}e^{-\epsilon\tau}, \tag{30}$$

where $\mathcal{F}_{SW}$ is the downwelling shortwave flux (in W/m^2), $\mathcal{S}$ the solar constant, τ the optical thickness, and ε the factor relating the longwave to shortwave optical thickness. Assuming that ε does not vary with pressure to first order, the shortwave flux convergence is simply given by

$$-\frac{d\mathcal{F}_{SW}}{dp} = \underbrace{\frac{\kappa\varepsilon f_1 f_2}{g}}_{\text{Diff opt thickness}} \mathcal{F}_{SW}. \tag{31}$$

In Appendix B2, we show that the linear shortwave response can be written as the sum of two terms:

$$\left(M_{SW}\right)_{ij} = \frac{\kappa\alpha_i \left(\mathcal{F}_{SW}\right)_{p_i}}{L_v} \underbrace{\left[\varepsilon f_1 \left(\frac{df_2}{dq}\right)_{q=0}\right]_{p_j}}_{\text{Opt thick pert}} \left[\underbrace{\delta_{ij}}_{\uparrow\text{Local emissivity}} - \frac{\overbrace{\kappa\Delta p \cdot \varepsilon \cdot \left(f_1 f_2\right)_{p_i}}^{\text{Local opt thickness}}}{g} \underbrace{\delta_{i<j}}_{\downarrow\text{Rad received}}\right], \tag{32}$$

1. A local increase in the radiative heating, due to the increase of the local emissivity.
2. A decrease in the solar radiation received below the perturbation level.

The shortwave linear response matrix is depicted in Figure 9b. The local increase in radiative heating corresponds to the red diagonal and is attenuated by the decrease in received solar radiation below the perturbation level. Because the atmosphere is optically thin in the shortwave, the strength of the linear response is mostly affected by the local value of the product αf_1, which increases strongly with pressure. Therefore, $\widehat{M_j}$ is greatest in the lower troposphere and quickly decays for higher perturbations. Although the gray model qualitatively exhibits the basic physics of the linear radiative response, different water vapor spectral bands saturate at different humidity levels, and we use of a full radiative model in order to yield accurate results in section 4.3.

4.3. Real-Gas Radiative Transfer

4.3.1. Method

In order to take into account the full water vapor absorption spectrum, we use the RRTMG model (Iacono et al., 2000, 2008; Mlawer et al., 1997) to compute the response of the atmosphere to small water vapor perturbations. Following Beucler and Cronin (2016), we use version 4.85 of the longwave and version 3.9 of the shortwave column versions of RRTMG, a broadband, two-stream, correlated *k*-distribution radiative transfer model that has been tested against line-by-line radiative transfer models. The RCE water vapor and temperature profiles are once again the observed January SAM RCE profiles and have 60 levels in the vertical. To match the clear-sky radiative transfer of the SAM base state as closely as possible, we also specify a constant carbon dioxide mixing ratio of 355 ppmv and use the standard SAM tropical ozone mixing ratio profile depicted in Figure 4d. The solar zenith angle is chosen to be $\arccos(\pi/4)$ rad, the insolation-weighted equatorial equinox value. The linear radiative responses are obtained in four steps:

1. We use RRTMG in order to compute the structure of the longwave and shortwave radiative fluxes from the RCE greenhouse gas and temperature profiles.
2. We perturb the RCE water vapor profile level by level. Sixty-four "moistened" profiles are produced, by adding 1% to the specific humidity at each level . Similarly, 64 "dried" profiles are produced by removing 1% from the RCE specific humidity at each level.
3. For each perturbed profile, we use RRTMG to compute the structure of longwave and shortwave radiative fluxes. We multiply the shortwave fluxes by a constant factor to account for the diurnal cycle and match the total shortwave heating in SAM (the factor is close to $4/\pi^2$, which would exactly account for an insolation-weighted zenith angle).
4. By subtracting the RCE radiative fluxes to the perturbed radiative fluxes, we obtain the perturbation radiative fluxes, from which we compute the longwave and shortwave linear responses matrices following equations (3) and (6).

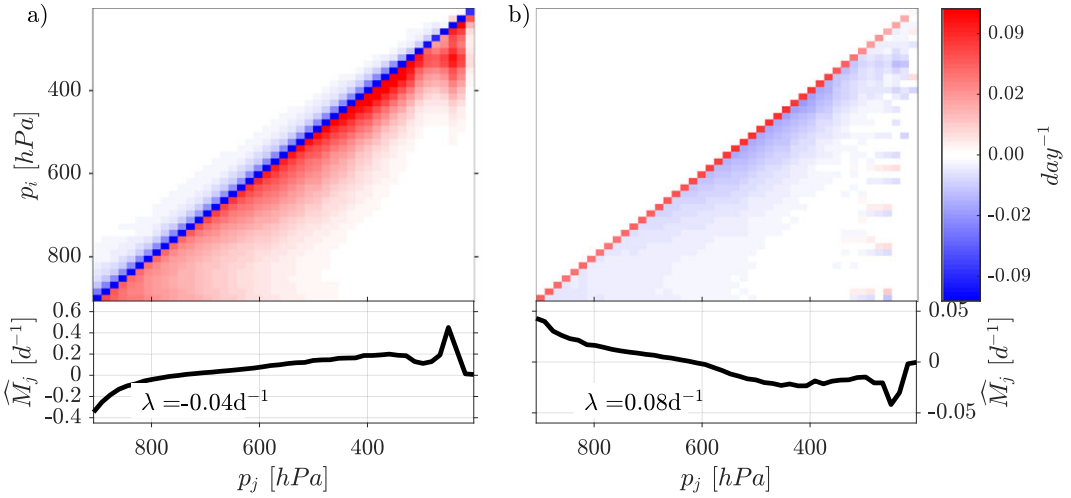

Figure 10. (a) Longwave linear response matrix (in month^{-1}) and vertically integrated longwave growth rate (in day^{-1}) plotted against perturbation level (in hPa). (b) Shortwave linear response and vertically integrated shortwave growth rate. The HAM has been evaluated from the reference SAM RCE profile. The leading real eigenvalue λ of each matrix is indicated in the corresponding bottom panel.

4.3.2. Results

The longwave and shortwave linear response matrices are respectively depicted in Figures 10a and 10b. The total radiative linear response matrix is qualitatively similar to the clear-sky radiative responses obtained by Emanuel et al. (2014) for a negative moisture perturbation, with a radiative amplification effect concentrated below the diagonal that expands as surface temperature increases. For the SAM RCE reference profile, the total longwave radiative cooling is 211 W/m^2 and the total shortwave radiative heating 61 W/m^2, leading to a net cooling of 150 W/m^2, which is the standard value we use for $\widehat{Q}_{BP}$ in the bulk-plume model (section 3.3). The vertically integrated response is negative for lower-tropospheric perturbations and grows as the longwave amplification effect becomes larger to values of order 0.5day^{-1} for perturbations near the tropopause. The shortwave effect is opposite and reaches −0.05 day^{-1} for perturbations near the tropopause. The main difference when going from a gray-gas to a real-gas model of radiation is the sharp amplification of the response growth rates near the tropopause. There, the most absorbing bands of water vapor (large κ) contribute to longwave cooling and shortwave heating. Therefore, small water vapor perturbations will change the optical thickness by a greater amount per unit mass perturbation in water vapor amount.

5. Linear Evolution of Small Water Vapor Perturbations

In this section, we combine the Betts-Miller convective response (referred to as BM, see section 3.2) and the bulk-plume convective response (referred to as BP, see section 3.3) with the real-gas radiative response (referred to as RRTM, see section 4.3), in order to obtain the full linear response and study the linear evolution of small water vapor perturbations. The total Betts-Miller response matrix $M_{BM+RRTM}$ and the total bulk-plume response matrix $M_{BP+RRTM}$ are given by

$$M_{BM+RRTM} = M_{BM} + M_{RRTM}, \tag{33}$$

$$M_{BP+RRTM} = M_{BP} + M_{RRTM}, \tag{34}$$

where M_{BM} is the Betts-Miller convective response (sum of the responses given by equations (12) and (13) for the Betts-Miller timescale τ_{BM} = 3hr, M_{BP} is the bulk-plume convective response (sum of the responses given by equations (23) and (24) for the radiative cooling parameter computed from the RRTM model, and M_{RRTM} is the RRTM radiative response (sum of the longwave and shortwave responses shown in Figure 10). We show in Appendix C that the results of this section are robust across a wide range of convective parameters τ_{BM} and $\widehat{Q}_{BP}$.

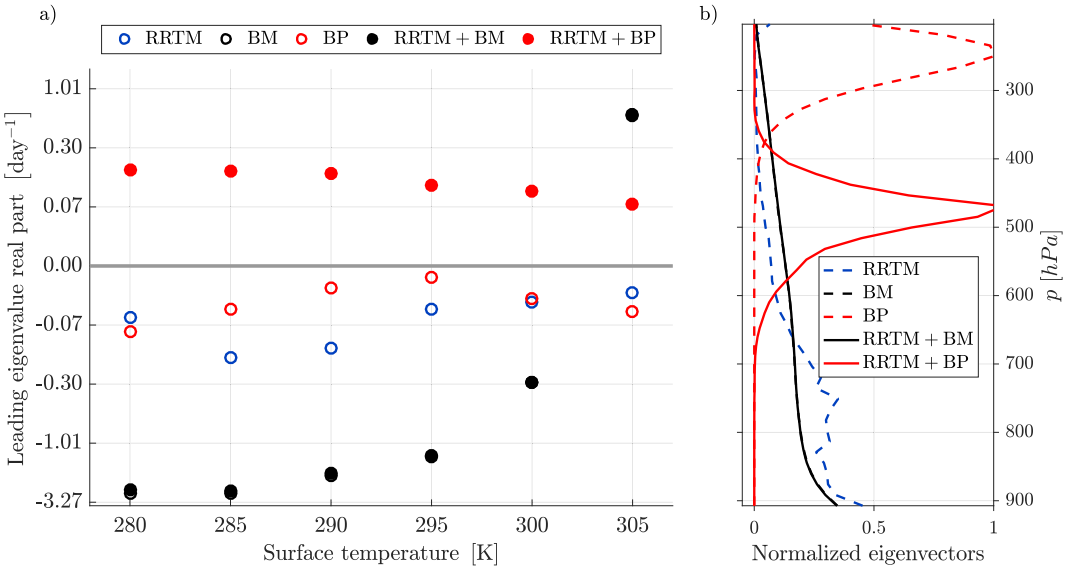

Figure 11. (a) Leading eigenvalue real part (in day^{-1}) as a function of the RCE surface temperature (in K). (b) Corresponding eigenvectors for the 300 K reference case: Radiative response alone (RRTM), Betts-Miller response alone (BM, $\tau_{BM} = 3$hr), bulk-plume response alone (BP, $\widehat{Q}_{BP} = 150$ W/m^2), and their sums (RRTM + BP) and (RRTM + BM). The lines for (BM) and (RRTM + BM) are indistinguishable. The eigenvectors have been normalized to have the same pressure average.

From section 2.1, we remember that the linear response matrix may be linearly unstable if its leading eigenvalue real part is greater than zero. In Figure 11a, we compute the leading eigenvalue real part of each matrix for different values of the surface temperature:

1. (RRTM) For the reference SAM RCE profile, the leading eigenvalue real part corresponds to a decay time scale of 27 days; there is no pure linear instability from radiation alone. Because the radiative linear response matrix is mostly lower triangular, with a strictly negative diagonal corresponding to strong local cooling, water vapor perturbations are displaced downwards and eventually damped out in the absence of convection, though they may initially amplify as they are displaced through nonnormal growth. Except for the 280 K case, the decay timescale increases with temperature, suggesting that the clear-sky radiation's damping effect is less pronounced in warmer climates. Finally, we find that the clear-sky radiative feedback can be linearly unstable if the RCE relative humidity profile is artificially dried, due to the upper-tropospheric radiative amplification effect. For readability purposes, the results are not shown in Figure 11 but provided to the reader in the corresponding MATLAB script.
2. (BM) In the WTG framework, Betts-Miller convection is linearly unstable if and only if the mean free-tropospheric HAM is larger than 1 (analogous to a negative gross moist stability). This condition is only satisfied for the 305 K simulation, in which the specific humidity remains above 5g/kg and the HAM remains above 1 in the lower troposphere (see Figures 4a and 4c). In the unstable case (305 K), the perturbation latent heating in the lower troposphere induces strong upward motion because $\alpha > 1$ there, leading to the unstable growth of lower to midtropospheric water vapor perturbations. In the stable case (all cases but 305K), these perturbations are damped because a larger mass of the atmosphere has: $\alpha < 1$, which makes the convective drying effect overcome the latent heating effect. Mathematically, we prove in Appendix A3 that the leading eigenvalue real part of the Betts-Miller linear response is proportional to the vertical average of HAM minus 1 (see equation (A9)), which increases with surface temperature as can be seen on Figure 11. This growth rate is exactly reached for a water vapor perturbation profile that is proportional to the HAM profile.
3. (RRTM+BM) Adding the radiative response reinforces the local and upper-tropospheric perturbation's damping. However, the stability of the combined linear response matrix is barely distinguishable from that of the convective response alone for Betts-Miller timescales as short as 3 hr.
4. (BP) The bulk-plume response is mostly upper triangular, with a strictly negative diagonal corresponding to local drying through the entrainment of the water vapor perturbation. The decay timescale of the

bulk-plume convective response is approximately equal to the minimal entrainment value, as the leading eigenvalue real part is close (within ∼20% in our case) to $-\min_p [e(p)]$, where e is the entrainment profile (see Appendix A3). Therefore, bulk-plume convection is always linearly stable on its own. The dependence of the leading eigenvalue real part on surface temperature is weak, consistent with the weak dependence of the entrainment minimum on surface temperature.

5. (RRTM + BP) The combination of the bulk-plume convective response with the radiative response is linearly unstable for all surface temperatures. Physically, lower-tropospheric perturbations are carried upwards by the plume where they can reinforce through the radiative amplification effect identified in equation (29). Upper-tropospheric perturbations can also amplify midtropospheric perturbations through radiative amplification, which are then carried upwards in the plume. Mathematically, the combination of an upper and a lower triangular matrices with positive off-diagonal values can allow part of the spectrum to become positive.

The leading eigenvalue real part informs us about the linear growth rate of each response matrix. We now focus on the vertical structure of water vapor perturbations. The evolution of a given perturbation can be found by exponentiating the linear response matrix, following equation (8). If we compute the growth rate of column water vapor perturbations, we find that the leading eigenvalue real part can be used as a predictor of the order of magnitude of the growth rate on a time scale of order days. For the first few hours, the transient growth rate of water vapor perturbations is very dependent on their initial shape. After a few days, dominant vertical modes appear, which mathematically correspond to the eigenvectors associated with the leading eigenvalue real part of each convective response. These eigenvectors, depicted in Figure 11b, are the HAM profile for M_{BM} and an upper tropospheric bulge for M_{BP}; they grow at a rate given by the corresponding leading eigenvalue real parts λ_{BM} and λ_{BP}. In contrast, the purely radiative response (RRTM) damps the perturbation in the upper troposphere, as radiative cooling is increased above the perturbation level, and in the lower troposphere, where the radiative amplification term is smallest. When combined with Betts-Miller convection (RRTM + BM), radiation slightly damps the upper-tropospheric perturbation, which can not be seen by eye in Figure 11b. However, the bulk-plume scheme moves the moist lower-tropospheric perturbation upwards in the midtroposphere, where the radiative amplification effect is largest. This means that the perturbation grows faster when bulk-plume convection and radiation are added (RRTM + BP). The perturbation decays in the lower troposphere, where it is entrained upwards, and in the upper troposphere, where it is advected downwards. In both cases, the convection scheme dominates the pattern of vertical moisture perturbation response. Thus, the (RRTM+BM) ς (BM) eigenvectors are indistinguishable, while the (RRTM+BP) ς (BP) eigenvectors are close in the lower troposphere. As a closing point, we remind the reader that these eigenvectors are all computed in terms of specific humidity; eigenvectors expressed in terms of relative humidity would in all cases be strongly weighted towards the upper troposphere, where the reference-state q is small.

6. Conclusion

In section 2, we developed a theoretical framework to compute the response of RCE to small water vapor perturbations in WTG: The resulting linear response function (equation (5)) is the sum of the convective moistening, convective heating, longwave heating and shortwave heating linear response functions. The linear response function can be represented as a two-dimensional matrix (equation (9)), which can be exponentiated in order to compute the evolution of water vapor perturbations for short times. In section 3, we calculated analytic responses of two toy models of the convective linear response: a Betts-Miller-like scheme, which redistributes a local moisture perturbation to the rest of the atmosphere in the form of convective heating, and a bulk-plume-like scheme, which sends a moisture perturbation upwards. Comparing our responses with those obtained by Kuang (2012; Figures 8c and 8d), the Betts-Miller response is similar to the response of a cloud-permitting model in an elongated domain (aspect ratio larger than 20), whereas the response of the same model in a square domain resembles the bulk-plume response. Additionally, the convective response studied in section 3.1.1 presents characteristics of both convective toy models, as confirmed by its eigenmode peaking at 575 hPa (right panel of Figure 3), which is the arithmetic mean of the bulk-plume's mode 250-hPa peak and the Betts-Miller's mode 90-hPa peak (right panel of Figure 11). This suggests that the physical insight obtained in section 3 could be used to understand the more intricate physics of cloud resolving model responses. In section 4, we investigated the physics of the clear-sky radiative response using the Schwarzschild equations. The response includes a local damping of moisture perturbations and a radiative amplification effect of midtropospheric perturbations in the lower troposphere.

We also quantitatively evaluated the clear-sky response by using a real-gas radiative transfer model and found large nongray radiative feedbacks in the upper troposphere. Section 5 shows that despite the damping effect of the radiative response, it could amplify the unstable convective response in the bulk-plume case. In contrast, the Betts-Miller response's stability depends on the mean free-tropospheric HAM, which increases with temperature, causing linear instability above surface temperatures of 300 K.

Although this work explores the physics of the interaction between water vapor, convection and clear-sky radiation in depth, two critical elements of the response are lacking: the cloud response and the surface temperature response. The first requires knowledge of how cloudiness responds to water vapor perturbations (which is mediated by convection and also depends on microphysical factors such as the background cloud condensation nuclei profile) and of how cloudiness affects the radiative heating profile. Preliminary results indicate that the cloud longwave response significantly enhances the longwave radiative amplification effect described in this study, making RCE more prone to linear instability. The second is an air-sea interaction problem, exploring the interaction between atmospheric moisture and surface temperature gradients, which could be relevant for monsoonal intraseasonal oscillations (e.g., Sengupta et al., 2001; Vecchi & Harrison, 2002) and help better understand coupled general circulation model results (e.g., Coppin & Bony, 2017).

This work connects with results from convection-permitting modeling by showing that despite the robustness of radiative thermodynamic feedbacks, the evolution and structure of water vapor perturbations is extremely sensitive to the linear response of convection. Even when convection is not parameterized, its linear response can differ greatly across model geometries (Kuang, 2012), and this may connect with the known sensitivity of aggregation to many aspects of convection-permitting model setup, including resolution and subgrid parameterizations (e.g., Muller & Held, 2012; Tompkins & Semie, 2017). Our findings may thus help to explain why the self-aggregation of convection in cloud-permitting models is finicky: The convective linear response is critical, and we still do not fully understand what controls it. Decomposing the full linear response into a Betts-Miller-type response, a bulk-plume-type response (using the mean HAM profile), and a radiative response could provide insight into the early stages of self-aggregation and help explain why the peak of the main moisture mode can be found in the midtroposphere.

Appendix A: Linear Response of the Bulk-Plume Equations

A1. Basic State

In order to eliminate the variations of the updraft mass flux m with pressure p, we combine equations (19)–(21) with equation (18):

$$gm\frac{\partial q^*}{\partial p} = c + eq_{\mathrm{def}}, \tag{A1}$$

$$gm\frac{\partial q}{\partial p} = dq_{\mathrm{def}}, \tag{A2}$$

$$gm\frac{\partial \left(s + L_v q^*\right)}{\partial p} = L_v eq_{\mathrm{def}}, \tag{A3}$$

where we have assumed that the in-cloud dry static energy was equal to the environmental dry static energy (neutral buoyancy assumption) and introduced the saturation deficit q_{def} defined in equation (22). Subtracting equation (A3) to equation (A2) and using equation (18) leads to a first-order differential equation for the updraft mass flux:

$$\frac{1}{m}\frac{\partial m}{\partial p} = -\frac{1}{q_{\mathrm{def}}}\left(\frac{\partial q_{\mathrm{def}}}{\partial p} + \frac{1}{L_v}\frac{\partial s}{\partial p}\right). \tag{A4}$$

The vertically integrated energetic balance requires that the free-tropospheric convective heating (equal to the convective flux at the top of the boundary layer) balances the free-tropospheric radiative cooling $\widehat{Q}_{\mathrm{BP}} > 0$:

$$\frac{L_v}{g}\int_{p_b}^{p} c = L_v m\left(p_b\right) q_{\mathrm{def}}\left(p_b\right) = \widehat{Q}_{\mathrm{BP}},$$

leading to the unique solution (18) for the updraft mass flux, as long as the free troposphere is not saturated in RCE ($\forall p,\ q < q^*$). The entrainment, detrainment and condensation rates can be obtained by combining equations (A3), (A2), and (A1) to equation (18).

A2. Linear Response

In order to compute the convective moistening and heating resulting from the moist perturbation q'_j, we follow the steps listed in section 3.3.3:

1. The convective drying tendency due to the entrainment of the moist perturbation in the plume can be written as follows:

$$\left(\frac{dq'_i}{dt}\right)_{\text{Ent}} = -e_j q'_j \delta_{ij}. \tag{A5}$$

2. The convective moistening due to the detrainment of water vapor from the plume (above the perturbation level) is

$$\left(\frac{dq'_i}{dt}\right)_{\text{Det}} = C_{\text{Det}} e_j q'_j d_i q_i^* \delta_{i>j}, \tag{A6}$$

while the convective heating due to the condensation of water vapor in the plume (above the perturbation level) is

$$L_v \left(\frac{dq'_i}{dt}\right)_{\text{Con}} = C_{\text{Con}} e_j q'_j c_i \delta_{i>j}, \tag{A7}$$

where C_{Det} and C_{Con} are proportionality constants. We have assumed that these two constants were equal ($C_{\text{Det}} = C_{\text{Con}} = C$). Using the conservation of the water vapor perturbation q'_j yields:

$$\left(\frac{dq'_i}{dt}\right)_{\text{Ent}} = \sum_{i>j} \left[\left(\frac{dq'_i}{dt}\right)_{\text{Det}} + \left(\frac{dq'_i}{dt}\right)_{\text{Con}}\right] \tag{A8}$$

Combining equations (A5)–(A8) allows us to express the proportionality constant C as a function of the detrainment and condensation rates:

$$C = \frac{1}{\sum_{i>j} \left(d_i q_i^* + c_i\right)}.$$

3. Step 5: The downwards advection of the perturbation by the subsidence mass flux can be written using an upwind advection scheme. At the perturbation level ($i = j$):

$$\left(\frac{dq'_i}{dt}\right)_{\text{Adv}} = -q'_j \frac{gm_j}{\Delta p} \delta_{ij},$$

while below the perturbation level ($i = j - 1$):

$$\left(\frac{dq'_i}{dt}\right)_{\text{Adv}} = q'_j \frac{gm_j}{\Delta p} \delta_{i(j-1)}.$$

The full convective moistening response (equation (23)) and convective heating response (equation (24)) are then computed by using their definition:

$$\left(M_{\text{LH}}\right)_{ij} = \frac{1}{q'_j}\left[\left(\frac{dq'_i}{dt}\right)_{\text{Ent}} + \left(\frac{dq'_i}{dt}\right)_{\text{Det}} + \left(\frac{dq'_i}{dt}\right)_{\text{Adv}}\right],$$

$$\left(M_{\text{DSE}}\right)_{ij} = \frac{\alpha_i}{q'_j}\left(\frac{dq'_i}{dt}\right)_{\text{Con}}.$$

Because of the limits of our simple bulk-plume model, the entrainment rate is negative right above the top of the boundary layer and in parts of the upper troposphere, which would yield inconsistent linear responses. This problem is addressed by replacing the negative values of e_j with the closest positive value of the entrainment rate that can be found below the level p_j.

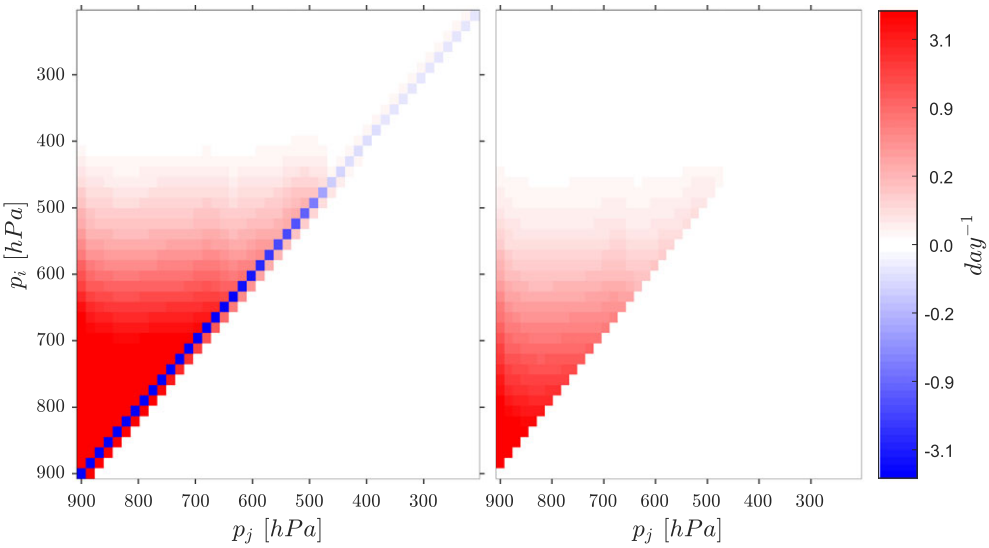

Figure A1. (a) Convective moistening (M_{LH}) and (b) Convective heating (M_{DSE}) linear response matrices, in units day^{-1}.

A3. Leading Eigenvalue of the Convective Response Matrices

We approximate the spectrum of the bulk-plume linear response matrix M_{BP} (sum of the responses given by equations (23) and (24) by the spectrum of the upper triangular matrix with the following diagonal:

$$\left(M_{BP}\right)_{ii} + \left(M_{BP}\right)_{(i-1)i} = -e_i.$$

In practice, this approximation is justified when the size of M_{BP} is large enough for its neighboring diagonal coefficients to be close:

$$\left|\left(M_{BP}\right)_{ii} - \left(M_{BP}\right)_{(i+1)(i+1)}\right| \ll \left|\left(M_{BP}\right)_{ii}\right|.$$

The spectrum of an upper triangular matrix is given by its diagonal values: $e_i > 0$, which means that the leading eigenvalue real part of the bulk-plume linear response λ_{BP} is approximately given by

$$\lambda_{BP} \approx -\min_p \left[e\left(p\right)\right].$$

For completeness, we compute the leading eigenvalue of the Betts-Miller linear response M_{BM} (sum of the responses given by equations (12) and (13). According to Gershgorin circle theorem, the spectrum of M_{BM} lies in the disc of center:

$$\left(M_{BM}\right)_{ii} = \frac{1}{\tau_{BM}}\left(-1 + \frac{\alpha_i \Delta p}{p_b - p_t}\right),$$

and radius

$$R_i = \sum_{j \neq i}\left|\left(M_{BM}\right)_{ij}\right| = \frac{\Delta p}{\tau_{BM}\left(p_b - p_t\right)}\sum_{j \neq i}\alpha_j.$$

Therefore, an upper bound for the real part of the spectrum of M_{BM} is

$$\lambda_{BM} = \left(M_{BM}\right)_{ii} + R_i = \frac{1}{\tau_{BM}}\left(\underbrace{\frac{\Delta p}{p_b - p_t}\sum_j \alpha_j}_{\text{Vertical average } \alpha} - 1\right). \tag{A9}$$

This upper bound is reached for the eigenvector α_i, which proves that λ_{BM} is the exact leading eigenvalue real part of the Betts-Miller linear response.

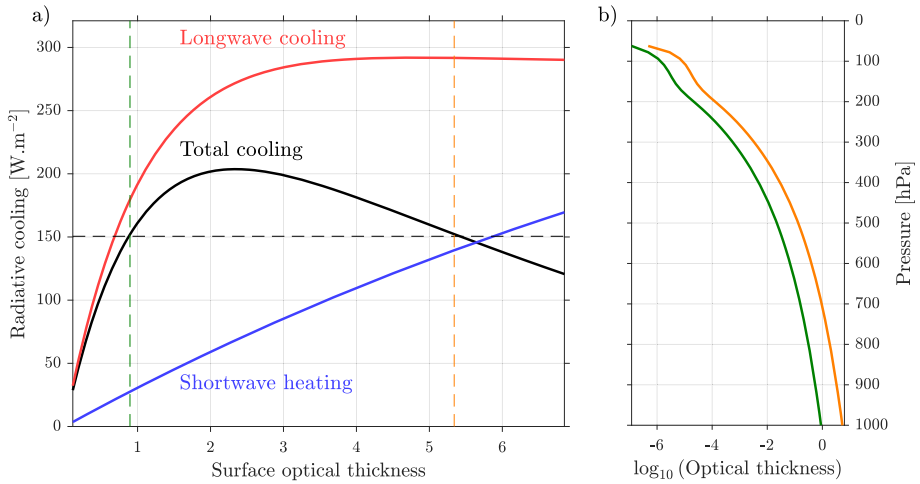

Figure A2. (a) Free-tropospheric longwave cooling (red line) and shortwave heating (blue line) and total net radiative cooling (black line) in W/m^2, versus surface optical thickness. The net radiative cooling in SAM is denoted with a dotted black line, and intersects the total radiative cooling of the gray model for two values of the surface optical thickness (denoted with green and orange vertical dotted lines). (b) Logarithm 10 of optical thickness profile in pressure space when the absorption coefficient is $\kappa = 0.022\,\mathrm{m}^2/\mathrm{kg}$ (green line) and $\kappa = 0.17\,\mathrm{m}^2/\mathrm{kg}$ (orange line).

Appendix B: Linear Response of the Schwarzschild Equations

B1. Two-Stream Model of Longwave Radiation

First, we linearize the longwave flux convergence, given by equation (26), about RCE:

$$\frac{g}{\kappa}\frac{d\mathcal{F}_{\mathrm{LW}}}{dp}' = f_1 f_2' \left(\mathcal{F}_\uparrow + \mathcal{F}_\downarrow - 2\sigma T^4\right) + f_1 f_2 \left(\mathcal{F}_\uparrow' + \mathcal{F}_\downarrow'\right) \quad , \tag{B1}$$

To quantitatively evaluate the second term of equation (B1), we can

1. Perturb the analytical solutions computed in Beucler and Cronin (2016) about RCE.
2. Use fundamental properties of the two-stream Schwarzschild equations, written below:

$$\frac{d\mathcal{F}_\uparrow}{d\tau} = \mathcal{F}_\uparrow - \sigma T^4 \quad , \quad \frac{d\mathcal{F}_\downarrow}{d\tau} = -\mathcal{F}_\downarrow + \sigma T^4. \tag{B2}$$

The first method is straightforward but mathematically technical; here we adopt the second method to gain physical insight into gray radiative transfer. Let us start with the upwelling flux $\mathcal{F}_\uparrow$ and integrate its Schwarzschild equation from the optical thickness τ_j of a level p_j to the optical thickness τ_i of a level p_i:

$$\underbrace{\left(\mathcal{F}_\uparrow\right)_{\tau_i}}_{\text{Flux i}} = \underbrace{e^{-(\tau_j-\tau_i)}}_{\text{Transmittivity i}\to\text{j}} \left[\underbrace{\left(\mathcal{F}_\uparrow\right)_{\tau_j}}_{\text{Flux j}} + \underbrace{\sigma \int_{\tau_i}^{\tau_j} T^4 e^{-\tau'} d\tau'}_{\text{Atm emission i}\to\text{j}} \right]. \tag{B3}$$

We now introduce an optical thickness perturbation τ_j' around the level p_j by introducing a water vapor perturbation q_j' in a thin pressure layer $[p_j - \Delta p/2\,,\ p_j + \Delta p/2]$ for which $\Delta p \ll p_j$. Our goal is to find the radiative response: $\left(\mathcal{F}_\uparrow + \mathcal{F}_\uparrow'\right)_{\tau_i}$ at the response level p_i. The bottom boundary condition is that the surface flux equals the (constant) terrestrial blackbody emission:

$$\left(\mathcal{F}_\uparrow\right)_{\tau_s} = \sigma T_s^4 = \left(\mathcal{F}_\uparrow + \mathcal{F}_\uparrow'\right)_{\tau_s + \tau_j'}.$$

We distinguish two cases:

1. If the perturbation level p_j is above the response level p_i, both the transmissivity and the atmospheric emission from the surface to the response level are unchanged. Writing equation (B3) between the surface and response levels shows that the radiative response is unchanged: $\left(\mathcal{F}'_{\uparrow}\right)_{\tau_i+\tau'_j} = 0$.
2. If the perturbation level p_j is below the response level p_i, we first write equation (B3) between the response level and right above the perturbation level:

$$\underbrace{\left(\mathcal{F}_{\uparrow}+\mathcal{F}'_{\uparrow}\right)_{\tau_i}}_{\text{Flux i}} = \underbrace{e^{-(\tau_j-\tau_i)}}_{\text{Transmittivity i}\to\text{j}}\left[\underbrace{\left(\mathcal{F}_{\uparrow}+\mathcal{F}'_{\uparrow}\right)_{\tau_j}}_{\text{Flux j}} + \underbrace{\sigma\int_{\tau_i}^{\tau_j} T^4 e^{-\tau'}d\tau'}_{\text{Atm emission i}\to\text{j}}\right], \tag{B4}$$

where the temperature profile in optical thickness space $T(\tau)$ is unperturbed because we are above the perturbation level. Subtracting equation (B3) to (B4) relates the perturbation fluxes at levels p_i and p_j:

$$\underbrace{\left(\mathcal{F}'_{\uparrow}\right)_{\tau_i}}_{\text{Perturbation flux i}} = \underbrace{e^{-(\tau_j-\tau_i)}}_{\text{Transmittivity i}\to\text{j}} \underbrace{\left(\mathcal{F}'_{\uparrow}\right)_{\tau_j}}_{\text{Perturbation flux j}}. \tag{B5}$$

Then, we write equation (B3) between the surface and right below the perturbation level, use the fact that the temperature profile does not change in pressure space, and use equation (B3) between the surface and level p_j before the perturbation was introduced:

$$\begin{aligned}
\underbrace{\left(\mathcal{F}_{\uparrow}+\mathcal{F}'_{\uparrow}\right)_{\tau_j+\tau'_j}}_{\text{Flux below pert}} &\overset{\text{Equation .12}}{=} \underbrace{e^{-(\tau_j-\tau_s)}}_{\text{Transmittivity s}\to\text{j}}\left[\underbrace{\left(\mathcal{F}_{\uparrow}+\mathcal{F}'_{\uparrow}\right)_{\tau_s+\tau'_j}}_{\text{Surface flux}} + \underbrace{\sigma\int_{\tau_j+\tau'_j}^{\tau_s+\tau'_j}\left(T+T'\right)^4 e^{-\tau'}d\tau'}_{\text{Atm emission s}\to\text{j}}\right] \\
&\overset{T(p)=(T+T')(p)}{=} \underbrace{e^{-(\tau_j-\tau_s)}}_{\text{Transmittivity s}\to\text{j}}\left[\underbrace{\left(\mathcal{F}_{\uparrow}\right)_{\tau_s}}_{\text{Surface flux}} + \underbrace{\sigma\int_{\tau_j}^{\tau_s} T^4 e^{-\tau'}d\tau'}_{\text{Atm emission s}\to\text{j}}\right] \\
&\overset{\text{Equation.12}}{=} \underbrace{\left(\mathcal{F}_{\uparrow}\right)_{\tau_j}}_{\text{Flux before pert}}.
\end{aligned} \tag{B6}$$

We can now express the perturbation flux at level j as a function of the total flux at level j to first order:

$$\begin{aligned}
\left(\mathcal{F}'_{\uparrow}\right)_{\tau_j} &\overset{\text{First order}}{=} \left(\mathcal{F}'_{\uparrow}\right)_{\tau_j+\tau'_j} \\
&\overset{\text{Equation.15}}{=} \left(\mathcal{F}_{\uparrow}\right)_{\tau_j} - \left(\mathcal{F}_{\uparrow}\right)_{\tau_j+\tau'_j} \\
&\overset{\text{First order}}{=} -\left(\frac{d\mathcal{F}_{\uparrow}}{d\tau}\right)_{\tau_j}\tau'_j \\
&\overset{\text{Equation.11}}{=} \left[\sigma T_j^4 - \left(\mathcal{F}_{\uparrow}\right)_{\tau_j}\right]\tau'_j \\
&\overset{\text{Equation 25}}{=} \left[\sigma T_j^4 - \left(\mathcal{F}_{\uparrow}\right)_{\tau_j}\right]\frac{\kappa\left(f_1 f'_2\right)_{\tau_j}}{g} \\
&\overset{\text{First order}}{=} \frac{\kappa}{g}\left(f_1\frac{df_2}{dq}\right)_{\tau_j}\left[\sigma T_j^4 - \left(\mathcal{F}_{\uparrow}\right)_{\tau_j}\right]q'_j \\
\left(\mathcal{F}'_{\uparrow}\right)_{\tau_j} &\overset{\text{Equation.14}}{=} \frac{\kappa}{g}\left(f_1\frac{df_2}{dq}\right)_{\tau_j} e^{-|\tau_i-\tau_j|}\left[\sigma T_j^4 - \left(\mathcal{F}_{\uparrow}\right)_{\tau_j}\right]q'_j
\end{aligned} \tag{B7}$$

It is possible to use a similar reasoning for the downwelling flux and find that:

1. If the perturbation level p_j is above the response level p_i, the downwelling flux is perturbed, and to first order:

$$\left(\mathcal{F}'_{\downarrow}\right)_{\tau_i} = \frac{\kappa}{g}\left(f_1\frac{df_2}{dq}\right)_{\tau_j} e^{-|\tau_i-\tau_j|}\left[\sigma T_j^4 - \left(\mathcal{F}_{\downarrow}\right)_{\tau_j}\right] q'_j. \tag{B8}$$

2. If the perturbation level p_j is below the response level p_i, the downwelling flux is unchanged.

Combining equations (B1), (B7), and (B8) leads to the longwave linear response (equation (27)) by using its definition:

$$\left(M_{\mathrm{LW}}\right)_{ij} \overset{\mathrm{def}}{=} \frac{g\alpha_i}{L_v q'_j}\left(\frac{d\mathcal{F}_{\mathrm{LW}}{}'}{dp}\right)_{p_i}. \tag{B9}$$

B2. One-Stream Model of Shortwave Radiation

First, we linearize the shortwave flux convergence, given by equation (31), about RCE:

$$-\frac{g}{\kappa}\frac{d\mathcal{F}_{\mathrm{SW}}{}'}{dp} = \varepsilon f_1 f'_2 \mathcal{F}_{\mathrm{SW}} + \varepsilon f_1 f_2 \mathcal{F}'_{\mathrm{SW}}, \tag{B10}$$

This time, we directly perturb the analytical solution for the downwelling shortwave flux:

$$\frac{\mathcal{F}_{\mathrm{SW}}}{\mathcal{S}} = e^{-\varepsilon\tau}, \tag{B11}$$

$$\frac{\mathcal{F}'_{\mathrm{SW}}}{\mathcal{S}} = e^{-\varepsilon\tau}\left(e^{-\varepsilon\kappa g^{-1}\int_0^p f_1 f'_2} - 1\right). \tag{B12}$$

Then again, we introduce a water vapor perturbation q'_j in a thin pressure layer $[p_j - \Delta p/2\,,\ p_j + \Delta p/2]$, for which $\Delta p \ll p_j$, and use the smallness of $\Delta p/p_j$ to simplify the form of the perturbation fluxes at a given level p_i:

$$\left(\frac{\mathcal{F}'_{\mathrm{SW}}}{\mathcal{S}}\right)_{p_i} = e^{-\varepsilon\tau_i}\frac{\varepsilon\kappa\Delta p}{g}\left(f_1 f'_2\right)_{p_j}\delta_{i<j}. \tag{B13}$$

Combining equations (B10) and (B13) leads to the shortwave linear response (equation (32)) by using its definition:

$$\left(M_{\mathrm{SW}}\right)_{ij} \overset{\mathrm{def}}{=} -\frac{g\alpha_i}{L_v q'_j}\left(\frac{d\mathcal{F}_{\mathrm{SW}}{}'}{dp}\right)_{p_i}. \tag{B14}$$

B3. Choice of the Optical Thickness

For consistency with Beucler and Cronin (2016), we represent the optical thickness for Figure 9 using the following functions of pressure in equations (25) and (30):

$$\kappa = 0.17\mathrm{m}^2/\mathrm{kg},\ \ f_1(p) = \frac{p}{p_s},\ \ f_2(q) = q,\ \ \varepsilon(p) \approx 0.077.$$

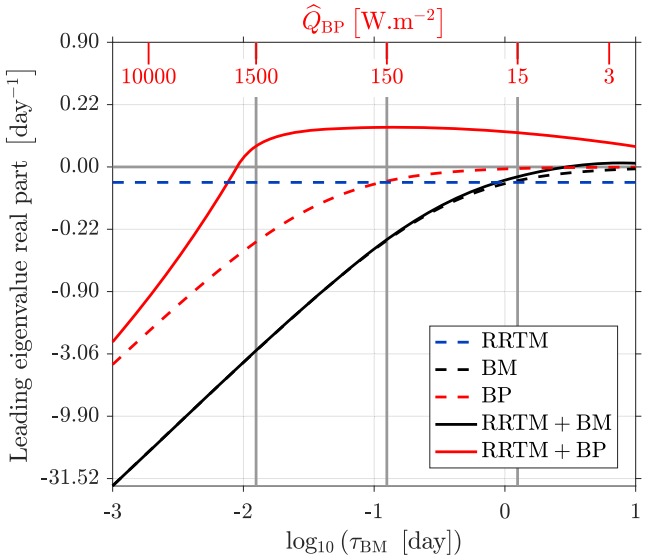

Figure C1. Leading eigenvalue real part of the 300 K linear response (in day^{-1}) as a function of $\log_{10} \tau_{\mathrm{BM}}$ (in hours, for the RRTM + BM and BM cases) and $\widehat{Q}_{\mathrm{BP}}$ (in W/m^2, for the RRTM + BP and BP cases). The scale for τ_{BM} and the scale for $\widehat{Q}_{\mathrm{BP}}$ are aligned so that the responses depicted on Figure 5 (BM, $\tau_{\mathrm{BM}} = 3$hr) and 7 (BP, $\widehat{Q}_{\mathrm{BP}} = 150$ W/m^2) fall on the same vertical line (central vertical gray line). The two other vertical gray lines indicate the range of realistic convective parameters.

This choice assumes a simple pressure broadening of water vapor, neglects the greenhouse effects of gas other than water vapor, and estimates the total shortwave absorption using equation (20) of Beucler and Cronin (2016). The net radiative cooling (sum of equations 17 and 21 in Beucler & Cronin, 2016) as a function of the free-tropospheric optical thickness is depicted in Figure A2, as well as its longwave and shortwave components. The net radiative cooling (black line) matches the radiative cooling computed by RRTM (150 W/m^2) for two choices of the absorption coefficient: $\kappa = (0.022\ ,\ 0.17)$ m^2/kg, corresponding to two surface optical thicknesses of $(0.8\ ,\ 5.4)$. For the gray radiative linear response matrix, we choose the optically thick solution $\kappa = 0.17$ m^2/kg (orange lines), for which the radiative cooling decreases with surface optical thickness and moisture radiative-cooling instability can occur (Beucler & Cronin, 2016).

Appendix C: Sensitivity to Convective Model Parameters

In this section, we investigate how the stability of the linear response depends on the convective parameters τ_{BM} and $\widehat{Q}_{\mathrm{BP}}$. Following section 5, we combine the Betts-Miller convective response and the bulk-plume convective response with the real-gas radiative response in order to obtain the full linear response and study the linear evolution of small water vapor perturbations. The total Betts-Miller response matrix $M_{\mathrm{BM+RRTM}}$ and the total bulk-plume response matrix $M_{\mathrm{BP+RRTM}}$ are given by

$$M_{\mathrm{BM+RRTM}}\left(\tau_{\mathrm{BM}}\right) = M_{\mathrm{BM}}\left(\tau_{\mathrm{BM}}\right) + M_{\mathrm{RRTM}}, \tag{C1}$$

$$M_{\mathrm{BP+RRTM}}\left(\widehat{Q}_{\mathrm{BP}}\right) = M_{\mathrm{BP}}\left(\widehat{Q}_{\mathrm{BP}}\right) + M_{\mathrm{RRTM}}, \tag{C2}$$

where the Betts-Miller convective response M_{BM} depends on the Betts-Miller timescale τ_{BM} and the bulk-plume convective response M_{BP} depends on the radiative cooling parameter $\widehat{Q}_{\mathrm{BP}}$, while the radiative response M_{RRTM} remains unchanged for a fixed surface temperature.

In Figure C1, we define the range of realistic convective parameters as τ_{BM} between 0.3 and 30 hr, and $\widehat{Q}_{\mathrm{BP}} = 150$ between 15 and $1,500$ W/m^2. Over this wide range of convective parameters, none of the leading eigenvalue real parts change sign. The combined RRTM and bulk-plume response is the only linearly unstable response with an average growth rate of 10.0 days over the realistic range of parameters.

Acknowledgments
We thank Zhiming Kuang for providing the data described in section 3.1.1, Tristan Abbott for providing the data described in section 3.1.2, Adam Sobel, and an anonymous reviewer for writing thoughtful and constructive reviews of the present manuscript. Tom Beucler thanks Rohini Shivamoggi for helpful suggestions that improved the clarity of the present manuscript. He also thanks Daniel Gilford and Marianna Linz for their help with the microphysics and statistical analysis tools that were used to analyze the results from the MIT Single Column Model. He was supported under NSF grants AGS-1136480 and AGS-1418508. Timothy W. Cronin was supported by NSF grant AGS-1623218. The source code and data used to produce the Figures can be found at https://github.com/tbeucler/Linear_response_framework_RCI, except for Figure 3's data, which was provided by Z. Kuang.

References

Adames, A. F., & Kim, D. (2016). The MJO as a dispersive, convectively coupled moisture wave: Theory and observations. *Journal of the Atmospheric Sciences*, *73*, 913–941. https://doi.org/10.1175/JAS-D-15-0170.1

Arakawa, A., & Schubert, W. H. (1974). Interaction of a cumulus cloud ensemble with the large-scale environment, Part I. *Journal of Atmospheric Sciences*, *31*, 674–701. https://doi.org/10.1175/1520-0469(1974)031<0674:IOACCE>2.0.CO;2

Betts, A. K., & Miller, M. J. (1986). A new convective adjustment scheme. Part II: Single column tests using GATE wave, BOMEX, ATEX and arctic air-mass data sets. *Quarterly Journal of the Royal Meteorological Society*, *112*(473), 693–709. https://doi.org/10.1002/qj.49711247308

Betts, A. K., & Miller, M. J. (1993). *The Betts-Miller Scheme* (pp. 107–121). Boston, MA: American Meteorological Society. https://doi.org/10.1007/978-1-935704-13-3_9

Beucler, T., & Cronin, T. W. (2016). Moisture-radiative cooling instability. *Journal of Advances in Modeling Earth Systems*, *8*, 1620–1640. https://doi.org/10.1002/2016MS000763

Bjerknes, J. (1938). Saturated-adiabatic ascent of air through dry-adiabatically descending environment. *Quarterly Journal of the Royal Meteorological Society*, *64*(2), 325–330.

Bretherton, C. S., Blossey, P. N., & Khairoutdinov, M. (2005). An energy-balance analysis of deep convective self-aggregation above uniform SST. *Journal of the Atmospheric Sciences*, *62*(12), 4273–4292. https://doi.org/10.1175/JAS3614.1

Chikira, M. (2014). Eastward-propagating intraseasonal oscillation represented by Chikira Sugiyama cumulus parameterization. Part II: Understanding moisture variation under weak temperature gradient balance. *Journal of the Atmospheric Sciences*, *71*(2), 615–639. https://doi.org/10.1175/JAS-D-13-038.1

Collins, W. D., Bitz, C. M., Blackmon, M. L., Bonan, G. B., Bretherton, C. S., Carton, J. A., et al. (2006). The community climate system model version 3 (CCSM3). *Journal of Climate*, *19*, 2122–2143. https://doi.org/10.1175/JCLI3761.1

Coppin, D., & Bony, S. (2017). Internal variability in a coupled general circulation model in radiative-convective equilibrium. *Geophysical Research Letters*, *44*, 5142–5149. https://doi.org/10.1002/2017GL073658

Emanuel, K., Wing, A. A., & Vincent, E. M. (2014). Radiative-convective instability. *Journal of Advances in Modeling Earth Systems*, *6*, 75–90. https://doi.org/10.1002/2013MS000270

Frierson, D. M. W. (2007). The dynamics of idealized convection schemes and their effect on the zonally averaged tropical circulation. *Journal of the Atmospheric Sciences*, *64*(6), 1959–1976. https://doi.org/10.1175/JAS3935.1

Grabowski, W. W., & Moncrieff, M. W. (2004). Moisture-convection feedback in the tropics. *Quarterly Journal of the Royal Meteorological Society*, *130*(604), 3081–3104. https://doi.org/10.1256/qj.03.135

Hannah, W. M., & Maloney, E. D. (2011). The role of moisture-convection feedbacks in simulating the Madden-Julian oscillation. *Journal of Climate*, *24*(11), 2754–2770. https://doi.org/10.1175/2011JCLI3803.1

Hartman, P. (1960). A lemma in the theory of structural stability of differential equations. *Proceedings of the American Mathematical Society*, *11*(4), 610–610. https://doi.org/10.1090/S0002-9939-1960-0121542-7

Herman, M. J., & Kuang, Z. (2013). Linear response functions of two convective parameterization schemes. *Journal of Advances in Modeling Earth Systems*, *5*, 510–541. https://doi.org/10.1002/jame.20037

Holloway, C. E., & Neelin, J. D. (2009). Moisture vertical structure, column water vapor, and tropical deep convection. *Journal of the Atmospheric Sciences*, *66*(6), 1665–1683. https://doi.org/10.1175/2008JAS2806.1

Holloway, C. E., & Woolnough, S. J. (2016). The sensitivity of convective aggregation to diabatic processes in idealized radiative-convective equilibrium simulations. *Journal of Advances in Modeling Earth Systems*, *8*, 166–195. https://doi.org/10.1002/2015MS000511

Iacono, M. J., Delamere, J. S., Mlawer, E. J., Shephard, M. W., Clough, S. A., & Collins, W. D. (2008). Radiative forcing by long-lived greenhouse gases: Calculations with the AER radiative transfer models. *Journal of Geophysical Research*, *113*, D13103. https://doi.org/10.1029/2008JD009944

Iacono, M. J., Mlawer, E. J., Clough, S. A., & Morcrette, J.-J. (2000). Impact of an improved longwave radiation model, RRTM, on the energy budget and thermodynamic properties of the NCAR community climate model, CCM3. *Journal of Geophysical Research*, *105*(D11), 14,873–14,890. https://doi.org/10.1029/2000JD900091

Inoue, K., & Back, L. (2015). Column-integrated moist static energy budget analysis on various time scales during TOGA COARE. *Journal of the Atmospheric Sciences*, *72*(5), 1856–1871. https://doi.org/10.1175/JAS-D-14-0249.1

Khairoutdinov, M. F., & Randall, D. A. (2003). Cloud resolving modeling of the ARM Summer 1997 IOP: Model formulation, results, uncertainties, and sensitivities. *Journal of the Atmospheric Sciences*, *60*, 607–625. https://doi.org/10.1175/1520-0469(2003)060<0607:CRMOTA>2.0.CO;2

Kuang, Z. (2010). Linear response functions of a cumulus ensemble to temperature and moisture perturbations and implications for the dynamics of convectively coupled waves. *Journal of the Atmospheric Sciences*, *67*(4), 941–962. https://doi.org/10.1175/2009JAS3260.1

Kuang, Z. (2012). Weakly forced mock Walker cells. *Journal of the Atmospheric Sciences*, *69*(9), 2759–2786. https://doi.org/10.1175/JAS-D-11-0307.1

Malkus, J. S., Ronne, C., & Chafee, M. (1961). Cloud patterns in Hurricane Daisy, 1958. *Tellus*, *13*(1), 8–30. https://doi.org/10.1111/j.2153-3490.1961.tb00062.x

Mapes, B., & Neale, R. (2011). Parameterizing convective organization to escape the entrainment dilemma. *Journal of Advances in Modeling Earth Systems*, *3*, M06004. https://doi.org/10.1029/2011MS000042

Mlawer, E. J., Taubman, S. J., Brown, P. D., Iacono, M. J., & Clough, S. A. (1997). Radiative transfer for inhomogeneous atmospheres: RRTM, a validated correlated-k model for the longwave. *Journal of Geophysical Research*, *102*(D14), 16,663–16,682. https://doi.org/10.1029/97JD00237

Muller, C., & Bony, S. (2015). What favors convective aggregation and why? *Geophysical Research Letters*, *42*, 5626–5634. https://doi.org/10.1002/2015GL064260

Muller, C. J., & Held, I. M. (2012). Detailed investigation of the self-aggregation of convection in cloud-resolving simulations. *Journal of the Atmospheric Sciences*, *69*, 2551–2565. https://doi.org/10.1175/JAS-D-11-0257.1

Pauluis, O. M., & Mrowiec, A. A. (2013). Isentropic analysis of convective motions. *Journal of the Atmospheric Sciences*, *70*(11), 3673–3688. https://doi.org/10.1175/JAS-D-12-0205.1

Plant, R. S. (2009). A review of the theoretical basis for bulk mass flux convective parameterization. *Atmospheric Chemistry and Physics*, *10*, 3529–3544. https://doi.org/10.5194/acpd-9-24945-2009

Ramanathan, V., & Coakley, J. A. (1978). Climate modeling through radiative-convective models. *Reviews of Geophysics*, *16*(4), 465–489. https://doi.org/10.1029/RG016i004p00465

Romps, D. M. (2014). An analytical model for tropical relative humidity. *Journal of Climate*, *27*(19), 7432–7449. https://doi.org/10.1175/JCLI-D-14-00255.1

Sengupta, D., Goswami, B. N., & Senan, R. (2001). Coherent intraseasonal oscillations of ocean and atmosphere during the Asian summer monsoon. *Geophysical Research Letters*, *28*(21), 4127–4130. https://doi.org/10.1029/2001GL013587

Singh, M. S., & O'Gorman, P. A. (2013). Influence of entrainment on the thermal stratification in simulations of radiative-convective equilibrium. *Geophysical Research Letters*, *40*, 4398–4403. https://doi.org/10.1002/grl.50796

Sobel, A. H., & Bretherton, C. S. (2000). Modeling tropical precipitation in a single column. *Journal of Climate*, *13*, 4378–4392. https://doi.org/10.1175/1520-0442(2000)013<4378:MTPIAS>2.0.CO;2

Sobel, A. H., & Gildor, H. (2003). A simple time-dependent model of SST hot spots. *Journal of Climate*, *16*, 3978–3992. https://doi.org/10.1175/1520-0442(2003)016<3978:ASTMOS>2.0.CO;2

Sobel, A. H., Nilsson, J., & Polvani, L. M. (2001). The weak temperature gradient approximation and balanced tropical moisture waves. *Journal of the Atmospheric Sciences*, *58*, 3650–3665. https://doi.org/10.1175/1520-0469(2001)058<3650:TWTGAA>2.0.CO;2

Stansifer, E. M., O'Gorman, P. A., & Holt, J. I. (2017). Accurate computation of moist available potential energy with the Munkres algorithm. *Quarterly Journal of the Royal Meteorological Society*, *143*(702), 288–292. https://doi.org/10.1002/qj.2921

Tompkins, A. M. (2001). Organization of tropical convection in low vertical wind shears: The role of cold pools. *Journal of the Atmospheric Sciences*, *58*, 1650–1672. https://doi.org/10.1175/1520-0469(2001)058<1650:OOTCIL>2.0.CO;2

Tompkins, A. M., & Semie, A. G. (2017). Organization of tropical convection in low vertical wind shears: Role of updraft entrainment. *Journal of Advances in Modeling Earth Systems*, *9*, 1046–1068. https://doi.org/10.1002/2016MS000802

Vecchi, G. A., & Harrison, D. E. (2002). Monsoon breaks and subseasonal sea surface temperature variability in the Bay of Bengal. *Journal of Climate*, *15*(12), 1485–1493. https://doi.org/10.1175/1520-0442(2002)015<1485:MBASSS>2.0.CO;2

Wing, A. A., Camargo, S. J., & Sobel, A. H. (2016). Role of radiative-convective feedbacks in spontaneous tropical cyclogenesis in idealized numerical simulations. *Journal of the Atmospheric Sciences*, *73*(7), 2633–2642. https://doi.org/10.1175/JAS-D-15-0380.1

Wing, A. A., & Cronin, T. W. (2016). Self-aggregation of convection in long channel geometry. *Quarterly Journal of the Royal Meteorological Society*, *142*(694), 1–15. https://doi.org/10.1002/qj.2628

Wing, A. a., & Emanuel, K. A. (2014). Physical mechanisms controlling self-aggregation of convection in idealized numerical modeling simulations. *Journal of Advances in Modeling Earth Systems*, *5*, 59–74. https://doi.org/10.1002/2013MS000269

Wing, A. A., Emanuel, K., Holloway, C. E., & Muller, C. (2017). Convective self-aggregation in numerical simulations: A review. *Surveys in Geophysics*, *38*, 1173–1197. https://doi.org/10.1007/s10712-017-9408-4

Wolding, B. O., Maloney, E. D., Henderson, S., & Branson, M. (2016). Climate change and the Madden-Julian Oscillation: A vertically resolved weak temperature gradient analysis. *Journal of Advances in Modeling Earth Systems*, *9*, 307–331. https://doi.org/10.1002/2016MS000843

Yanai, M., Esbensen, S., & Chu, J.-H. (1973). Determination of bulk properties of tropical cloud clusters from large-scale heat and moisture budgets. *Journal of Atmospheric Sciences*, *30*, 611–627. https://doi.org/10.1175/1520-0469(1973)030<0611:DOBPOT>2.0.CO;2

Yu, J.-Y., Chou, C., & Neelin, J. D. (1998). Estimating the gross moist stability of the tropical atmosphere. *Journal of the Atmospheric Sciences*, *55*(8), 1354–1372. https://doi.org/10.1175/1520-0469(1998)055<1354:ETGMSO>2.0.CO;2